Ocean Engineering 291 (2024) 116412

Contents lists available at ScienceDirect

Ocean Engineering

journal homepage: www.elsevier.com/locate/oceaneng

A general FSI framework for an effective stress analysis on composite wind turbine blades

ZhongSheng Deng [a], Qing Xiao [a,*], Yang Huang [a], Liu Yang [b], YuanChuan Liu [c]

[a] Department of Naval Architecture, Ocean & Marine Engineering, University of Strathclyde, Glasgow, UK
[b] Department of Mechanical & Aerospace Engineering, University of Strathclyde, Glasgow, UK
[c] College of Engineering, Ocean University of China, Qingdao, China

ARTICLE INFO

Handling Editor: Prof. A.I. Incecik

Keywords:
FSI
CFD
FEA
Composite blades
Stress analysis

ABSTRACT

The fluid-structure interaction (FSI) technique has been extensively used and developed in the past decades. Commonly, the reduced-order models are used in FSI analyses to assure the numerical robustness and efficiency. However, due to the increasing demand for higher numerical resolutions in modern wind turbine composite blade applications, intrinsic limitations of reduced-order models, such as their inability to account for complex aerodynamic flow interactions, multi-motion couplings, and sophisticated composite properties, have become the weaknesses in existing reduced-order FSI approaches. In this study, we propose a general FSI framework, which combines the advantages of high-fidelity Computational Fluid Dynamics (CFD) and robust Multi-Body Dynamics (MBD) methods, and detailed Finite Element Analysis (FEA) for analysing the detailed stress distributions on the composite structures. The results of predicted dynamics and the Von Mises stress on the composite blade structures under given operation condition are compared and reasonably agreed with the literature results, with a significant computational cost reduction by nearly 25% is achieved. The proposed FSI framework can be a general approach to investigate the multi-physical interactions where the composite structure specifications are involved, coupling with complex dynamic motions in three-dimensional space.

1. Introduction

Wind turbine blades play a crucial role in extracting wind energy. With the increasing trend of scaling up modern wind turbines, there has been a growing need to enhance the structural strength of composite blades. According to the Global Wind Energy Council (Mark and Feng, 2023), the global grid-connected wind turbine capacity has increased to approximately 906 GW in 2022. The wind energy market is still expanding rapidly. It is expected that in 2023, a new installed global wind turbine capacity will exceed 100 GW for the first time. This rapid growth in the wind energy market would inevitably lead to an increasing demand for blade design, testing, inspection, and optimization.

One of the key aspects of investigating the modern composite blade structural performances is to analyse the blade dynamic responses, under specified operation conditions. To do so, among the existing numerical analysing methods, the FSI approaches have been extensively adopted and justified to be a reliable way for the structural performance evaluation of the wind turbine blade.

Modern composite blades feathered on large-scale wind turbines consist of multiple materials, such as carbon-fibre-reinforced polymers (CFRP), glass-fibre-reinforced polymers (GFRP), polyurethane foam, and resin, etc. (Zhang et al., 2023). The mechanical properties of these materials, as well as factors like the stacking sequence, stacking locations, in-ply fibre angles designs, and the numbers of laminate layers are crucial determinants of the blade's structural performance. Due to these factors, the numerical analysis of blade structural performance can be complicated during the numerical modelling processes.

Many numerical studies have extensively utilized reduced-order FSI approaches to investigate the flexible blade dynamic response of NREL 5 MW wind turbine blade (Cheng et al., 2019; Dose et al., 2018; Liu et al., 2019; Yu and Kwon, 2014; Yu et al., 2020), while only a few FSI studies have investigated the blade structural performance, combining high resolution aerodynamics and fully resolved composite structures on the blade (Miao et al., 2019; Wang et al., 2016b).

In reduced-order FSI approaches, the flexible blade aero-elastic performances are analysed with high efficiency by sacrificing certain level of fidelity of the systems in fluid or structure participants. For example, in the fluid participant, semi-empirical models such as the

* Corresponding author.
E-mail address: qing.xiao@strath.ac.uk (Q. Xiao).

https://doi.org/10.1016/j.oceaneng.2023.116412
Received 14 September 2023; Received in revised form 30 October 2023; Accepted 18 November 2023
Available online 27 November 2023

blade-element momentum (BEM) and free-vortex wake model (FVW) are frequently used for the blade aerodynamic predictions. And for the structural participant, the structural dynamics can be well predicted by one-dimensional (1D) Euler-Bernoulli beam models or multibody dynamics models (Masarati et al., 2014). Riziotis et al. (2008) investigated the nonlinearities of the blade structure under large deflections using reduced-order FSI, where the blade aerodynamics were accounted by the BEM model, and the blade structural behaviour was produced using beam element multibody model with different number of orders. The bending-torsion of the blade due to the deflections was captured and a reasonable aeroelastic response was provided. Lago et al. (2013) updated the BEM with linear operators, with corrections of the tip losses and the skewed wake phenomenon (Rahimi et al., 2016), making the BEM achieves a better performance in capturing the transient aerodynamic loads on the blades under the rotation conditions. The slender blade structure was considered with a reduced-order beam element model, specifically, the stiffnesses along the cross-sections on the one-dimensional beam model was equivalised based on the actual three-dimension elastic blade cross-section profile, so that the anisotropic properties and nonlinear dynamics of the actual composite blade were taken into account in a 1D beam element blade model (Cesnik and Hodges, 1997).

Many of these reduced-order fluid models require certain corrections to achieve a good performance in aerodynamics predictions. For instance, the BEM model is incapable of considering problems involving complicated turbulence effects and the transient flow interactions in three-dimensional (3D) space. For such method to achieve better flow predictions, correction models need to be found via comprehensive experimental investigations (Lanzafame and Messina, 2012; Sayed et al., 2019; Sharifi and Nobari, 2013), especially when the geometry or the fluid flowing conditions are complicated. Therefore, reduced-order fluid models like BEM are incapable of being a general model when analysing problems of wind turbine aerodynamics considering the turbulent flows under complex motions coupling scenarios.

To obtain a more realistic predictions of the blade aerodynamics, Yu and Kwon (2014) adopted the blade surface resolved CFD with rotationally periodic boundary conditions and non-linear Euler-Bernoulli cantilever beam model in their loose coupling FSI, as the fluid and structural participants, respectively. The predicted NREL 5 MW wind turbine time-averaged aerodynamic results were compared with FAST-Aerodyn (Jonkman et al., 2009) with good agreements. Similarly, Dose et al. (2018) and Liu et al. (2019) both analysed the aeroelastic performance of the NREL 5 MW wind turbine under the rated operation conditions, considering the turbulence, boundary layer flow and pressure distributions on the blade surfaces using high-fidelity CFD in their FSI approach. The overall structural responses, i.e., translational and rotational displacements of the blade were also well captured using the beam-element-based structure solver. However, the composite material mechanical properties were not considered in their methods, which is a pronounced limitation that needs to be improved for the needs of a higher resolution of the blade structure field. Therefore, a better way to achieve this goal is to use FEA approach to resolve the stress/strain distributions and local stress concentration on the composite material blade.

Attempt has been made to adopt a fully resolved finite element (FE) model in a two-way FSI analysis coupling with high-fidelity CFD. Bazilevs et al. (2011) developed a strong-coupling FSI procedure that combines the blade surface resolved CFD and an isogeometric finite element non-uniform rational B-splines (NURBS) structure model to accurately predict the aerodynamics and structural performance of a NREL 5 MW wind turbine blade. A single orthotropic material property was considered in their structural model, with a non-uniform thickness variation being resolved for illustrating a nonlinear stress distribution along the blade. However, the composite materials anisotropic properties with multiple layup configurations were not presented. To simplify the structural modelling process, the blade components such as the spar caps and shear webs were excluded in their studies.

Miao et al. (2019) investigated the NREL 5 MW wind turbine blades' load mitigating performance with different blade bend-twist strategies and the effects of composite fibre angle for the blade load mitigation. The extreme wind condition of the DLC 6.1 (design load case) – a 50-year extreme steady wind state was considered (Resor, 2013). Taking advantages of the FE model, detailed stress information, such as the stress concentration and distributions on the composite blades with 4 different composites stacking strategies were resolved and compared, where the maximum stress was observed at the near root region on the suction side of the blade.

Although a much more comprehensive representation of the blade aeroelastic performances can be achieved in a fully resolved high-fidelity CFD-FEA two-way FSI, the computational cost of such approach is usually massive (Wang et al., 2016a). This is because in high-fidelity FSI approaches, to achieve a robust and accurate coupling requires a strict control of matching of physical interfaces and intensive numerical interpolations between the involved solvers, which could be numerically challenging and infeasible in terms of computational efficiency, especially when complicated physical conditions need to be considered. This may explain why the studies using such approach are absent.

Another attempt has made by Wang et al. (2016b), where a one-way FSI procedure was established for the structural analysis of the composite blade. A fully resolved composite blade FE model was built. To fulfil the consideration of blade rotations in CFD, a 120-degree 'wedge' shaped mesh domain was used, with a periodic boundary condition applied to simulate for the blade aerodynamics during rotation cycles. Although the one-way FSI outperforms the two-way FSI approach in terms of computational efficiency, the only transferred field quantity during a one-way FSI process is the aerodynamic force, whereas the structural dynamic responses were omitted during the communications between the fluid and structure fields. This may bring some deficiencies to the accuracies of numerical prediction depending on the complexity and the sensitivity of the coupled physical fields, usually depends on the problem that is being analysed. If the fluid flowing characteristics are significantly relevant to the dynamic changes of the physical boundary, especially when the large structural deformation exists, a one-way FSI seems not to be an applicable choice for the aeroelastic analysis under such case.

Given the discussions above, the aim of this paper is to develop a general FSI framework considering the 3D, composite structures, time-dependent aerodynamics for analysing the stress on a wind turbine blade application, as an extension of our previous work (Liu et al., 2019). This framework integrates the advantages of 1) the high-fidelity CFD for realistic time-varying aerodynamic predictions; 2) a computational efficient two-way FSI procedure couples with multibody dynamics model for an accurate prediction of the structural dynamics; and 3) a fully resolved FEA analysis providing detailed stress field distributions on the composite structures.

In the following, Section 2 introduces the establishment of the proposed FSI framework for the stress analysis, the numerical formulations in fluid and structure models and the FSI coupling procedures; Section 3 demonstrates a simple test to justify the feasibility of the proposed FSI framework; Section 4 describes the NREL 5 MW baseline wind turbine composite blade geometry CAD model and finite element model in Abaqus CAE; and in Section 5, two different load cases are analysed for the composite blade using the proposed FSI framework, the aerodynamic and structural performance in both fields will be investigated with detailed stress field resolved on the flexible blade composite structures.

2. Methodology

The presented FSI framework is based on a strong-coupling two-way FSI approach, which has been well established in our previous work by

Liu et al. (2019). Main functionalities of the FSI approach are well preserved, while the features are extended, so that the actual composite structure stiffness properties in 3D space can be considered and resolve for the detailed stress distributions on composite structures.

2.1. Architecture of the FSI framework

This sub-section introduces how the three advantages as mentioned previously are integrated in the proposed stress analysis framework. The architecture of the proposed FSI framework is presented in Fig. 1. At the beginning of the analysis, the fully resolved FE model is firstly established in Abaqus CAE. Following with 3 main procedures, ending with the stress field establishing procedure in Abaqus CAE, which completes the analysing procedures.

In Procedure 1, the structural properties of the FE model are extracted and preserved as the intermediate datasets of the composite structural mass properties (CSMP) and the effective stiffness matrices (ESMs) of each partitioned section of the FE model in Abaqus. The ESMs are processed using the VABS code (Cesnik and Hodges, 1997; Chen et al., 2010; Yu et al., 2002), where the mechanical properties of the composite structure FE model in 3D space can be accounted by the ESMs in the beam model, which is used by the multibody dynamics model of MBDyn (Masarati et al., 2014) in Procedure 2.

Then, in Procedure 2, the strong-coupling two-way FSI analysis is conducted, where the transient aerodynamic loads with turbulent effects can be considered by high-fidelity CFD, and the dynamic performance of the structure under aerodynamic conditions are solved by multibody dynamics model in MBDyn. The structure inertial, centrifugal, deformational response can be well captured during the FSI coupling.

With Procedure 1 and 2, the actual macroscopic structural response can be accounted by the beam model in MBDyn in a strong-coupling two-way FSI. Unlike the direct CFD-FEA FSI coupling, the proposed procedures would perform more efficient, since the outstanding computational costs and strict controlling of coupling interface are avoided.

Finally, in Procedure 3, the displacements preserving macroscopic structure dynamic response solved by MBDyn will be explicitly interpolated onto the blade FE model as the boundary condition (BC) in the Abaqus static structure analysis, to establish the Von Mises stress field in the composite blade FE model.

The Von Mises stress is an equivalent stress which combines the influence of both normal principal stresses and shear stresses on the material. By comparing the Von Mises stress on the simulated material against the experimental results, it evaluates the material stress condition under specified loads, so that the potential vulnerable locations of material and structure can be identified.

In this procedure, the displacement fields solved by MBDyn during the strong-coupling FSI process can accurately reflect the blade nonlinear structure responses at arbitrary moments, under any operation conditions with or without complex motion couplings. Factors such as the moment of inertia, the centrifugal and gravitational effects, and the additional excitations due to the active rotor rotation, can be well preserved and reflected in the structural displacement data. In the scope of present FSI framework for stress analysis, the adoption of displacement is faster in terms of operations. A precise control and calibration of the displacement distribution on the structures is easier to be realised comparing with that using the force field. Therefore, it shows a better applicability and precision for establishing the stress fields using the displacement fields in the scope of our proposed framework.

2.2. Numerical modelling in OpenFOAM

2.2.1. Governing equations

The Unsteady Reynolds-Averaged Navier-Stokes equations (URANS) are adopted in OpenFOAM 4.0 (Jasak et al., 2007) to handle the fluid turbulence behaviour. The closure of URANS is realised by implementing the k-ω SST turbulence model (Menter et al., 2003). This is a well-known turbulence model in capturing complex flow behaviours during the transitioning process of the flow shedding from the blade surface to the wake region. The conservation governing equations for a control volume in the differential form are:

$$\nabla \cdot \boldsymbol{U} = 0 \tag{1}$$

$$\frac{\partial \boldsymbol{U}}{\partial t} + \nabla \bullet (\boldsymbol{U} - \boldsymbol{U}_g)\boldsymbol{U} = -\frac{\nabla p}{\rho} + \nabla \bullet \left[\nu_{eff} \nabla \boldsymbol{U} + (\nabla \boldsymbol{U})^T\right] \tag{2}$$

where $\boldsymbol{U}$ is the flow velocity in controlled volume, $\boldsymbol{U}_g$ is the velocity of moving grid nodes. p is the pressure of the fluid, ρ and stands for the fluid density. Due to the mesh dynamic motions, in the diffusion term, a treatment to account for the viscous stress tensor is made, using effective kinematic viscosity ν_{eff} which is the sum of kinematic (ν) and eddy viscosity (ν_t), respectively.

2.2.2. Solver and dynamic mesh

The transient pimpleDyMFoam solver (Carneiro et al., 2019; Liu et al., 2019; Wang et al., 2012) is adopted to solve the pressure and velocity fields of the flow, where the mesh motions can be introduced with the corrected surface flux solved on a moving grid in a transient simulation. The PIMPLE pressure-velocity coupling scheme is implemented. A second-order discretizing scheme is applied for both temporal and spatial terms to achieve better control of the potential numerical diffusion during the iterative process.

The Arbitrary Mesh Interface (AMI) technique (Chandar and Gopalan, 2016) is implemented to enable the relative sliding motions (rotations) of the wind turbine blades. The wind turbine rotor is included in a partitioned slave cell zone, where the designated angular speed of the wind turbine rotor can be assigned. The field quantities are transferred via a patch face-weighted interpolation between the master and slave interfaces on the AMI patches. A robust interpolation is maintained throughout the simulation, realised by the in-house code library (Liu et al., 2019), which prevents the deterioration of the mesh quality due to any undesired mesh penetration across the AMI during the iterating process.

During the FSI process, the flexible blade structure is exposed under

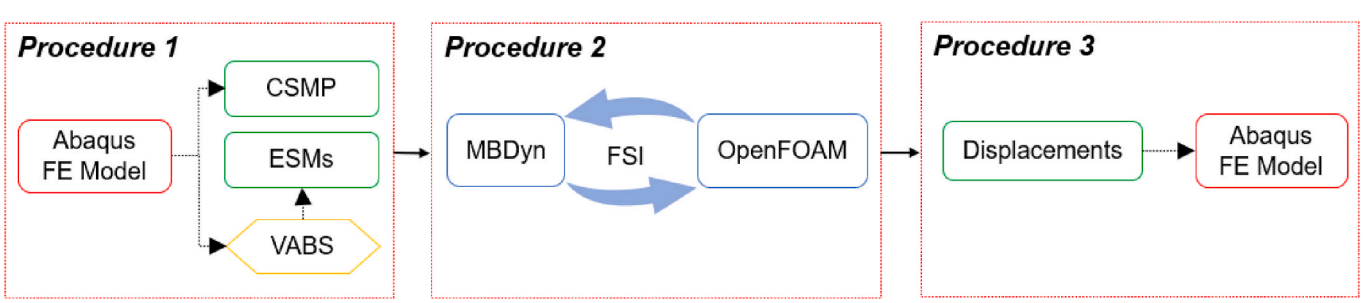

Fig. 1. Diagram of the proposed FSI framework of stress analysis.

the transient aerodynamic loads, resulting dynamic response usually with nonlinear displacement distributions on the structure. To capture the deformations of the blade, the mesh nodes on the blade surfaces need to be updated via a diffusive model by solving the inverse distance Laplace equation in each coupling iteration (Jasak and Tukovic, 2006):

$$\nabla \bullet (\gamma \nabla \boldsymbol{u}) = 0, \gamma = \frac{1}{r^2} \tag{3}$$

where $\boldsymbol{u}$ denotes the displacement vector of the mesh node on target wall surface, γ stands for the diffusivity coefficient which is calculated as the quadratic inverse of the node offset distance r from its original cell centroid to the deformed location. The mesh topology remains unchanged throughout the FSI process to ensure the consistency of the mesh sequencing and no additional interpolations are required, which performs more efficient comparing with other dynamic meshing algorithms such as remeshing and overset meshing techniques.

2.3. Numerical modelling in structure

Two structure solvers are involved in the proposed framework. As mentioned previously in sub-section 2.1, the FE model in Abaqus is essential as it firstly offers datasets of ESMs and CSMP for the use in MBDyn for a more computational efficient FSI analysis, allowing it to provide accurate structural macroscopic responses. Then, the structural responses of displacements are extracted from MBDyn and used as boundary conditions in Abaqus for resolving the stress on the FE model. The modelling formulations of both solvers are introduced below.

2.3.1. MBDyn – participant in FSI

In Procedure 2 of the proposed framework, the structural code MBDyn is used in the FSI process to predict structural response. The structural elasticity is considered by the lumped-parameter model incorporating into the beam-element multibody dynamics. The Newton-Euler motion equations subjected to the holonomic constrains are formulated in a differential-algebraic form, described as (Haug, 2016; Shabana, 2020; Simeon, 2006):

$$\boldsymbol{M}\dot{\boldsymbol{x}} = \boldsymbol{p} \tag{4}$$

$$\dot{\boldsymbol{p}} + \varphi_x^T \boldsymbol{\lambda} = \boldsymbol{f}(\boldsymbol{x}, \dot{\boldsymbol{x}}, t) \tag{5}$$

$$\varphi(\boldsymbol{x}, t) = 0 \tag{6}$$

where, $\boldsymbol{M}$ is the inertia matrix of the nodal system; the dot operator calculates the derivative of the variable with respect to time; $\boldsymbol{x}$ is a generalized form of nodal coordinates in global system; $\boldsymbol{p}$ is the nodal momentum vector. $\boldsymbol{f}$ denotes the external force and moment; the term φ_x^T denotes the Jacobian matrix of the constraint equations with respect to $\boldsymbol{x}$, and $\boldsymbol{\lambda}$ is the Lagrange multipliers calculating the reaction force under the given constraints.

A series of three-node beam element are facilitated for discretizing the structure in MBDyn. The complete axial and shear constitutive properties are defined on the midpoints of the three-node beam for the integrations of force, and subsequently solve the nodal translational and rotational displacements. Equipping with the diagonal ESMs and CSMP, the anisotropic properties of the structures with composite layups can be accounted by the beam-element model in MBDyn, where the structural dynamic responses can be accurately captured.

2.3.2. Abaqus – finite element model

In Abaqus CAE, the fully resolved finite element model of the composite blade is built up. To resolve the plane normal and curvature variations along the blade geometry surface, a general-purpose with finite-strain hypothesis S4R element is selected for the conventional shell modelling of the discretized blade in Abaqus. S4R (4-nodes shell element with reduced integration) is suitable for modelling composite structures for wind turbine blades and effectively avoiding transverse shear locking, and no need to concern about the potential hourglassing phenomenon (SIMULIA, 2014). The shape function in the S4R shell element extrapolates of nodal displacements, and subsequently obtains the strain tensor fields of the discretized model.

Given that the composite laminate exhibits orthotropic macroscopic mechanical properties, there is no coupling between the components of stresses and strains on the principal axial and transverse shear directions, besides, the in-plane shear stresses have no effects to the strains in other orthogonal planes. The linear elastic constitutive of the materials defined in Abaqus CAE is formulated as the following assembled compliance matrix with 6 independent variables:

$$\begin{Bmatrix} \varepsilon_1 \\ \varepsilon_2 \\ \gamma_{12} \end{Bmatrix} = \begin{bmatrix} 1/E_1 & -\nu_{12}/E_1 & 0 \\ -\nu_{12}/E_1 & 1/E_2 & 0 \\ 0 & 0 & 1/G_{12} \end{bmatrix} \begin{Bmatrix} \sigma_{11} \\ \sigma_{22} \\ \tau_{12} \end{Bmatrix} \tag{7}$$

Or, in a simple form to describe the strain – stress relation:

$$\varepsilon_i = C_{ij}\sigma_j \tag{8}$$

where the matrix includes two in-plane Young's modulus in 2 orthogonal directions E_1, E_2; Poisson's ratio ν_{12} (ν_{21} is implicitly defined as $\nu_{21} = (E_2/E_1)\nu_{12}$); and Shear modulus G_{12}, in addition, two other shear modulus G_{13}, G_{23} are required when the transverse shear needs to be calculated in shell models.

2.4. FSI coupling between OpenFOAM and MBDyn

To guarantee the convergence during the FSI coupling process, multiple inner and outer iterating loops are applied with given residual error limits within each coupling timestep, controlled by the in-house code library based in OpenFOAM developed by Liu et al. (2019), which accounts for the interpolation control and stabilization.

2.4.1. Coupling procedure

The complete coupling procedure is illustrated in Fig. 2. As the FSI coupling starts, the communications of the participants are firstly established via the TCP/IP socket on the same port. Then, solvers will be called which initiates the calculations and synchronizations of both participants. At every time step, the convergence of aerodynamic loads and structural responses are achieved in a partitioned way in OpenFOAM and MBDyn, respectively. This process keeps looping until the stopping conditions are met.

2.4.2. Data interpolation

Fig. 3 reflects a clearer data interpolating relation between the fluid and structural solvers. The mesh surface in the OpenFOAM is partitioned into several sections named $patch_{N-1}$, $patch_N$ and $patch_{N+1}$, aligning in accordance with MBDyn structure nodes of $node_{N-1}$, $node_N$ and $node_{N+1}$, placing at the corresponding patch aerodynamic centres for maintaining the interpolation accuracy for both forces and displacements.

Take $patch_{N-1}$ as an example, as the simulation begins in OpenFOAM, an integration of force F_{N-1} is calculated on $patch_{N-1}$ and will be directly transferred to MBDyn structure $node_{N-1}$. Similarly, the integrated aerodynamic load on each OpenFOAM patch is subsequently passed to corresponding MBDyn structure node, so that the structural response can be solved and provides the updated nodal displacement of motions.

To illustrate the interpolation process of displacement transfer for an arbitrary mesh node on the patches, an example of surface node A0 (star) locates on the yellow patch is used. The updated of motion for the surface node A0 is realised by a bilinear distance-weighted interpolation method, which transfers MBDyn node dynamics to OpenFOAM blade surface mesh for the mesh updates, formulated as:

$$\boldsymbol{K} = \alpha(\boldsymbol{k}_{i-1} + \boldsymbol{R}_{i-1}\boldsymbol{d}_{i-1}) + (1-\alpha)(\boldsymbol{k}_i + \boldsymbol{R}_i\boldsymbol{d}_i) \tag{9}$$

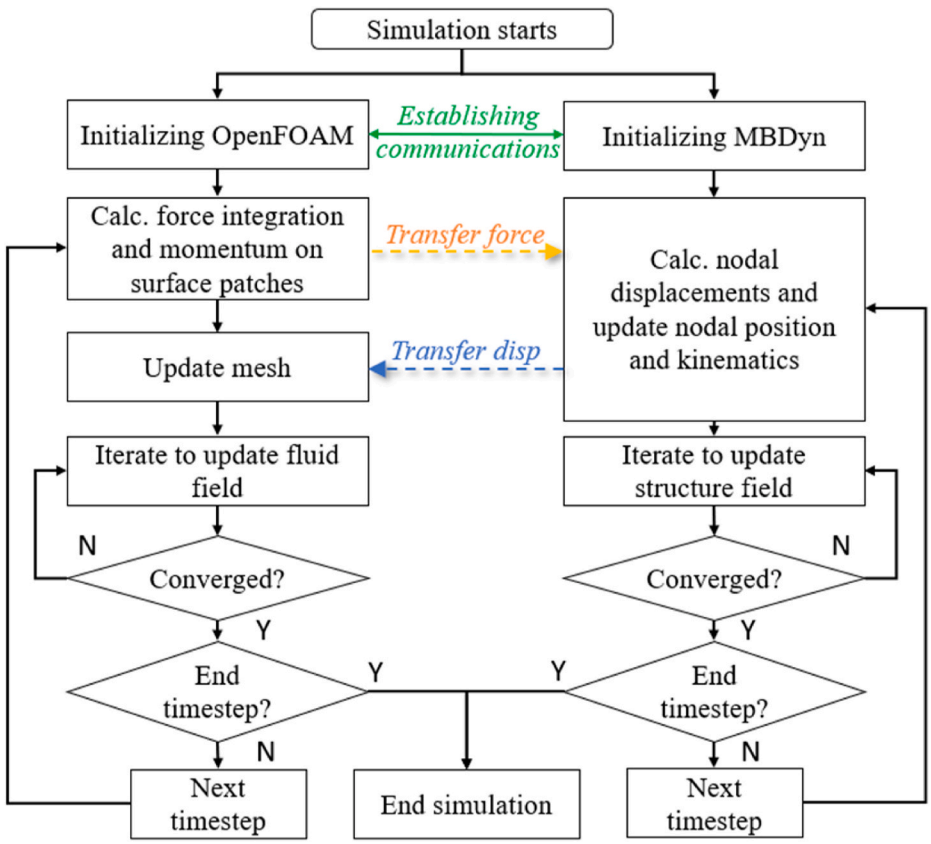

Fig. 2. Schematic diagram of the two-way FSI coupling procedures between OpenFOAM and MBDyn.

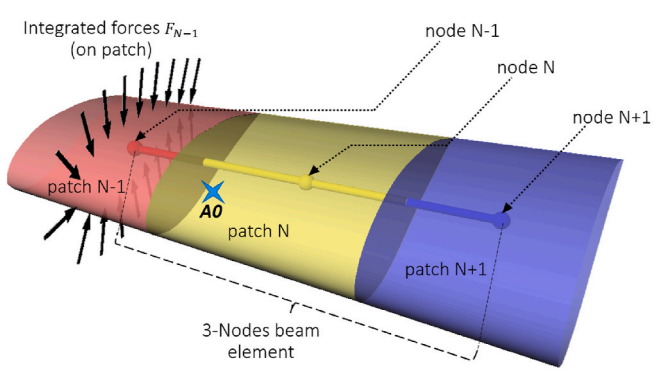

Fig. 3. Diagram of data interpolations between participants in the present study.

where $\boldsymbol{K}$ denotes the updated coordinates of node A0; $\boldsymbol{k}$ represents the translation of the patch centre (i.e. MBDyn structure nodes); $\boldsymbol{R}$ denotes the quaternion matrices, accounting for the node transformations due to the rotation of structure nodes; $\boldsymbol{d}$ stands for the distance vector pointing from the patch centre to the surface node A0; $\boldsymbol{n}$ is the vector pointing from its adjacent structure Node i-1 to Node i; and α is the weight for the dynamics interpolations onto the blade surface node, calculated by the distance projection from $\boldsymbol{d}$ to $\boldsymbol{n}$, as:

$$\alpha = \frac{\boldsymbol{n} \bullet \boldsymbol{d}}{|\boldsymbol{n}|^2} \tag{10}$$

3. Feasibility study

A feasibility study is conducted on a composite cylindrical tube FE model with shell element to demonstrate the validity and applicability of the proposed displacement mapping procedure, as it is the key step for resolving the stress fields on general shapes of geometry FE models.

The tube dimensions and composite material specifications are displayed in Fig. 4. The length of the tube $L = 61.5\ m$, with a diameter of $d = 5\ m$ are assigned which resembles a similar scale of the wind turbine blade that is analysed in this paper. The unidirectional glass and carbon fibre laminates are applied on the tube, where the laminar properties are specified as shown in Fig. 5. An even thickness of t = 0.047 m is assigned for each laminate, uniformly distributed along the tube model.

Preliminarily, the tube is partitioned into 25 sections in both MBDyn and Abaqus FE models for the convenience of the boundary conditions assignments, and to firstly determine whether the number of partitioning nodes is sufficient enough to capture the stress distribution properly, where the number of partitioned sections can be further increased if the load condition is expected to be complex. The locations of each partitioning nodes on the tube axial direction (Z coordinate) are displayed in Fig. 4.

The tube FE model is established in Abaqus. Subsequently, the tube sectional CSMP acquired from the tube FE model, with the ESMs calculated using VABS are applied on the beam model in MBDyn, as shown in Fig. 6. The diagonal form of ESM is listed in Table 1.

As depicted in Figs. 5 and 6, the static analyses are conducted on both Abaqus FE model and MBDyn beam model, where at top of the tube, a concentrated constant force of 100 kN on X direction is applied. At bottom of the tube, a fixed BC is applied locking all nodal Degrees of Freedom on the bottom edge. A Path containing a series of nodes of interest is defined for plotting the flapwise displacement distributions along the tube, denoted in red dash line.

The flapwise displacements predicted by Abaqus and ESMs-equipped MBDyn are firstly compared to examine the consistency of two solvers in structural responses predictions. As shown in Fig. 7, the flapwise displacement distributions predicted by both solvers agrees well with

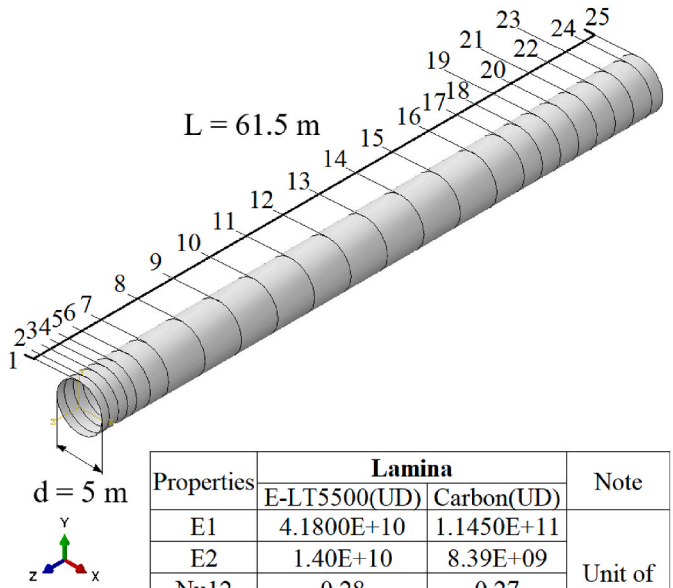

Properties	Lamina		Note
	E-LT5500(UD)	Carbon(UD)	
E1	4.1800E+10	1.1450E+11	Unit of modulus: Pa
E2	1.40E+10	8.39E+09	
Nu12	0.28	0.27	
G12	2.63E+09	5.99E+09	
G13	2.63E+09	5.99E+09	
G23	5.4688E+09	3.3032E+09	

Partitioning nodes ID	location on tube axial direction (Z coord, m)
1	61.5
2	60.7
3	59.7
4	58.7
5	57.7
6	56.2
7	54.2
8	50.2
9	46.2
10	42.2
11	38.2
12	34.2
13	30.2
14	26.2
15	22.2
16	18.2
17	15.2
18	13.2
19	11.2
20	9.2
21	7.2
22	5.2
23	3.2
24	1.2
25	0

Fig. 4. Tube dimensions and specifications for the numerical feasibility study.

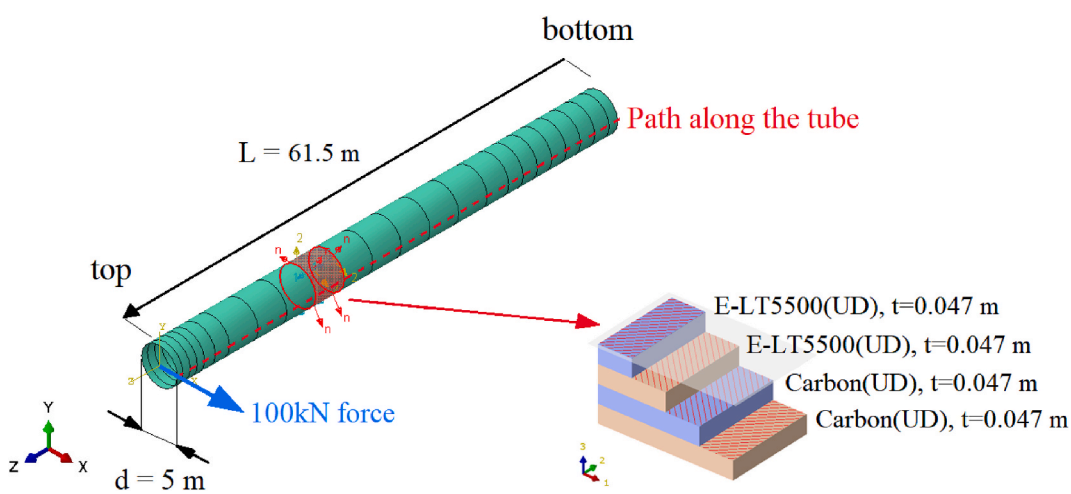

Fig. 5. Diagram of tube dimensions, composite layups and load condition of the FE model in Abaqus.

each other, meaning the 3D composite structural properties of the tube can be accurately preserved by the ESMs-equipped 1D beam model in MBDyn, providing close predictions of structural response as it would performs in a FE model.

Meanwhile, the stress field on the tube FE model under the concentrated force has been solved in Abaqus, as displayed in Fig. 8 (a1). Then, with the displacement field acquired from the MBDyn, the stress field is established via the displacement mapping procedure, as shown in Fig. 8 (a2). The horizontal axis denotes the percentage of the circumference of the unfolded tube, beginning at the middle left of the cross section, with an anti-clockwise precession to complete a full cycle of the circumference, as denoted in Fig. 6.

From Fig. 8 (a1), the stress concentration locates at the bottom of the tube where the spanwise distance is 1.282 m, at symmetrical positions of 0% and 50% of the circumference. A rapid stress gradient variation is found around the stress concentration location. In the stress field resolved by the displacements, as shown in Fig. 8 (a2), the stress concentration is found to be located in the similar region at the bottom of the tube. The stress distribution in both stress fields performs similar in the region where the tube spanwise distance $l > 10\ m$.

An underestimation of Von Mises stress concentration is found, as shown in Fig. 8 (b), where a deviation of predicted maximum stress of both stress fields is $\Delta\sigma_{max} = 14\ \%$. Given that the stress fields are solved with different boundary conditions through different procedures, it is inevitable that certain discrepancies would arise in two stress distributions.

From the comparisons, it is considered that the disparity of the maximum Von Mises stresses magnitudes between two stress fields remains in an acceptable range, with a reasonable agreement in stress distributions on the Path along the tube, proving that the proposed FSI framework is feasible to obtain the stress distributions on a composite structure as demonstrated on a tube model. It is anticipated that, by increasing the number of partitioned sections, the maximum stress deviation could be further mitigated and performs better in capturing the

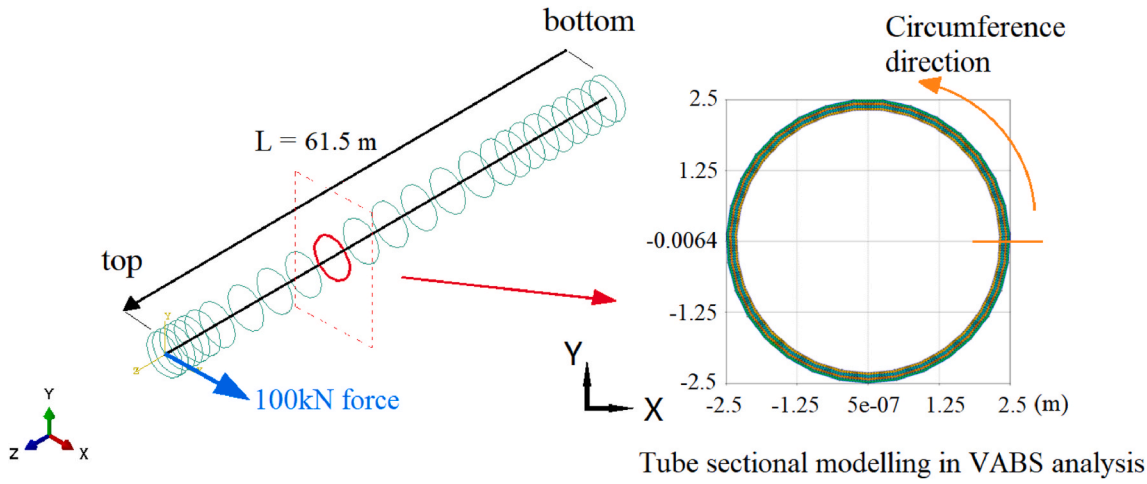

Fig. 6. Diagram of tube model in MBDyn, equipped with ESMs from VABS analysis.

Table 1
ESM of the composite tube in diagonal form.

Extension Stiffness-EA (Pa)	torsional stiffness-GJ (Pa)	Principal bending stiffness-EI22 (Pa)	Principal bending stiffness-EI33 (Pa)	Principal shear stiffness-GA22 (Pa)	Principal shear stiffness-GA33 (Pa)
4.1813E+10	2.9959E+10	2.9959E+10	3.5083E+11	1.2211E+11	1.2211E+11

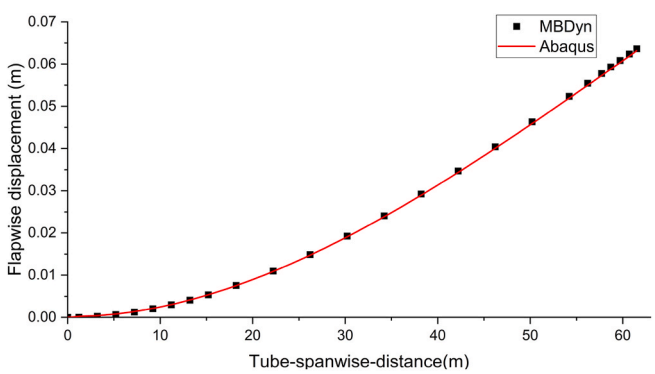

Fig. 7. Comparisons of flapwise displacement distributions on the Path predicted by Abaqus FE model and MBDyn beam model.

rapid stress gradient around the stress concentration location.

4. NREL 5 MW wind turbine composite blade FE model

The proposed generalized FSI framework for stress analysis is applicable for a series of problems that involves FSI analysis for composite structures. To further illustrate its capability in analysing for the composite wind turbine blade applications, in this section, the NREL 5 MW baseline wind turbine composite blade is analysed.

The designed blade length is $R = 61.5$ m. Considering the potential numerical divergence due to large mesh distortion under severe load conditions, a truncation at the sharp blade tip region is implemented during the modelling process, so that a satisfying mesh quality can be guaranteed. This leads to the final blade length in the present model is $R' = 59.8$ m.

Fig. 9 shows the generation process from blade CAD to its FE model. The designated blade profiles adopted by the blade are shown in Fig. 9 (a), including DU and NACA series airfoils (Resor, 2013). Fig. 9 (b) shows fifty partitioning surfaces for intercepting the intermediate blade cross sections for a smoother transitional shape and thickness variations along the blade. From the cross-sectional view (A-A') in Fig. 9 (c), the chordwise stacking partitioning areas are displayed, including: the leading edge (LE), leading edge panel (LE_Panel), Spar Cap (Cap), trailing edge panel (TE_Panel), trailing edge reinforcement (TE_Reinf) and trailing edge (TE). Additionally, the shear webs (SW1, SW2) which are the main supporting component to endure the shear stress under the aerodynamic loads. Fig. 9 (d) demonstrated the completed blade model, applied with composite stacks and non-uniform distributed sectional dimensions.

The composite laminate layer stackings along the blade are configurated based on the number of layers as shown in Fig. 10, thereby, it can be seen that the blade geometry is divided into multiple regions in spanwise, result in a non-uniform thickness distribution along the blade. A well arrangement of composite stacking sequence and number of layers variations on both spanwise and chordwise for each partitioned area is crucial. Any misalignment in material stacking orders can result in inaccurate blade mass and stiffness properties.

The material properties of the involved composite laminates can be found in the official document by Resor (2013). Before validating the blade mass properties and modal frequencies, a mesh convergence study is finalized by examining the maximum Von Mises stresses magnitude under a constant flapwise tip displacement of 5 m. Three different mesh element sizes are tested for the blade FE model, listed in Table 2. It is found that the element size of 0.10 m enables a balance of accuracy and computational efficiency.

The mass properties of the blade FE model are firstly compared. As shown in Table 3, the blade mass is slightly underestimated by approximately 1.71 %, also for the mass centre with a 3.35% underestimation, where the mass centre shifts on the spanwise direction of 0.685 m lower. Table 4 and Fig. 11 display the comparisons of modal frequency tests (1-6th modes), and the modal shapes of the composite blade FE model, respectively. Good agreements are achieved with an acceptable deviation less than 5% for all predicted modal frequencies, comparing to the results provided by Resor (2013).

5. Case studies

Two case studies are conducted for the NREL 5 MW baseline wind turbine under the extreme design load case (DLC) 6.1 condition (Case 1),

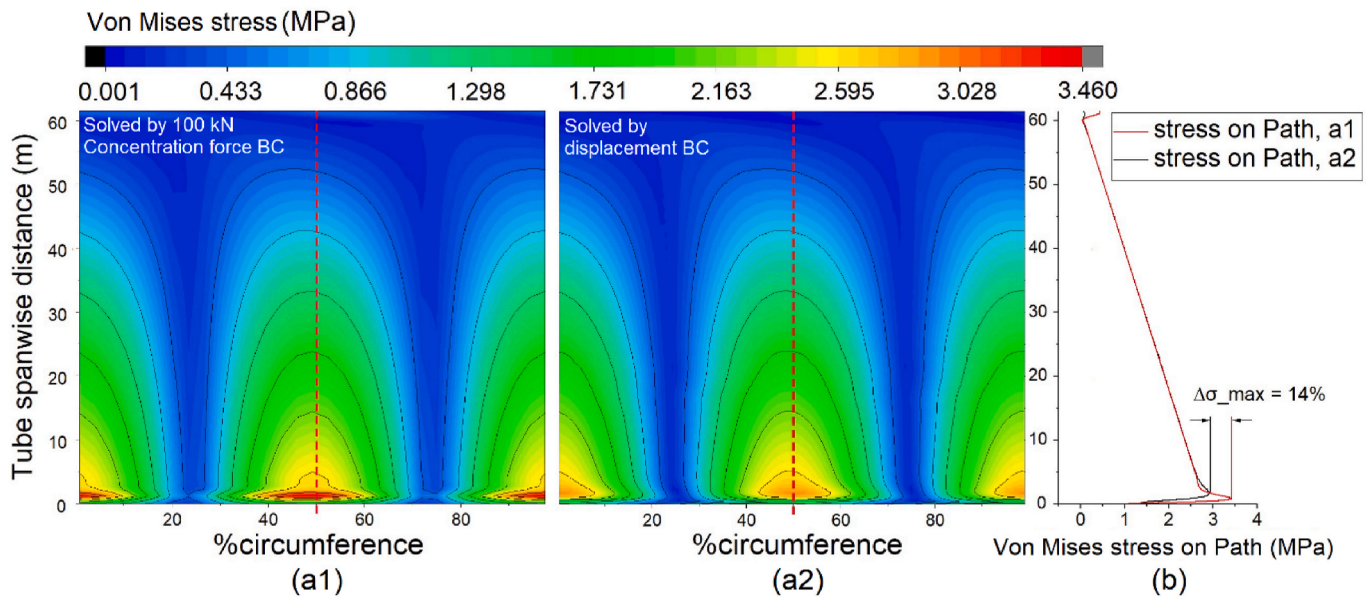

Fig. 8. Von Mises stress contours on the unfolded cylinder surface, solved by (a1) Abaqus –stress field resolved under the 100 kN concentration force; (a2) Abaqus –stress field resolved under displacements acquired from the ESMs-equipped MBDyn; (b) Comparison of the Von Mises stress distributions along the Path.

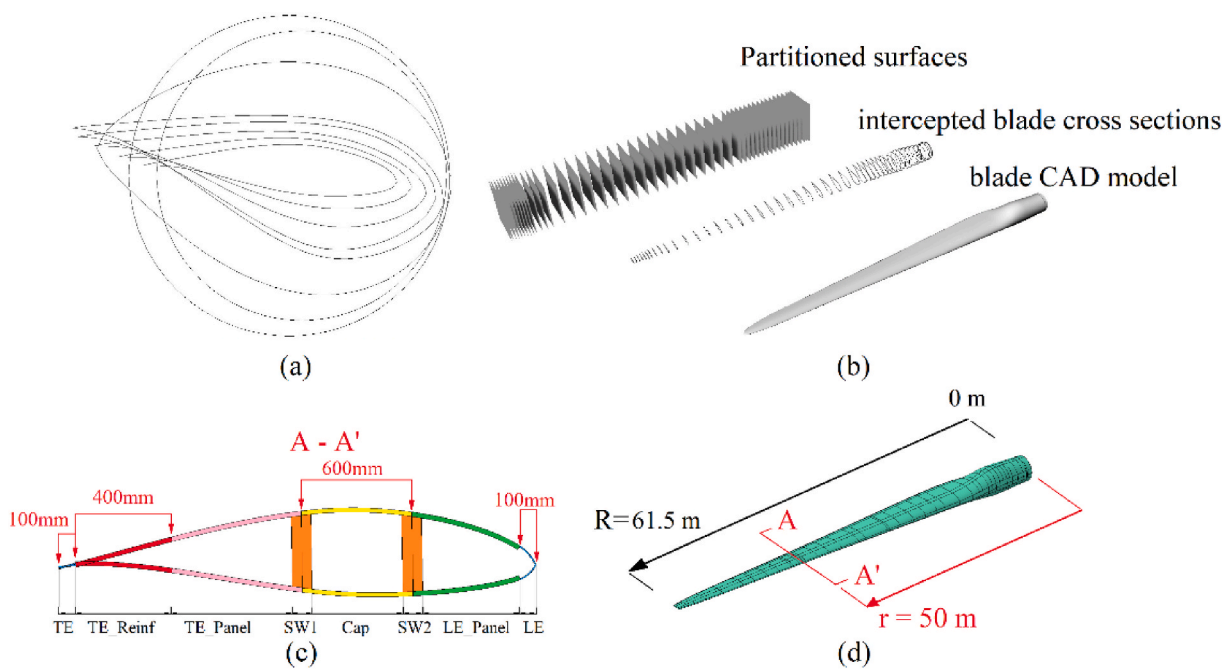

Fig. 9. (a) The designated airfoils on the blade, (b) CAD model of the blade geometry, (c) Local partitioning on a blade cross section, NACA 64–618 airfoil, and (d) Blade FE model with A-A′ plane depicted on blade spanwise r/R = 81.3%.

and the rated operation condition (Case 2).

In Case 1, the aerodynamics and structural response of the composite blade is analysed and compared to the results from Miao et al. (2019). In Case 2, the blade aeroelastic behaviours are investigated, detailed fluid field and structural stress field on the composite blade are examined.

5.1. Model specifications

The full-scale NREL 5 MW wind turbine blade mesh in CFD model is generated using the snappyHexMesh meshing utility. The tower and nacelle are not included in the model to minimise the complexity of the mesh. In the blade CFD mesh, the blade precone and pitch angle, and the rotor axial tilt angle are set to zero degree.

The centre of the rotor is placed at the coordinate origin (0, 0, 0) in the global system as shown in Fig. 12. The domain dimensions on X, Y, and Z directions are ranged from −1.5D to 1.5D, where D= 126 m is the diameter of the rotor. The blockage effect is neglected as the inlet and all the side boundaries are treated as the uniform velocity inlet condition, enclosed by the outlet where a zero-gradient pressure condition is applied. A regional refinement is implemented in the rotating cell zone to assure a proper capture of the flowing behaviours. In the near wall region, a boundary layers y+ in a range between 30 and 300 is assigned, so that the wall functions are applied to account for the viscous flow in the boundary layer. The characteristic cell size is $\Delta d = 0.0625$ m to

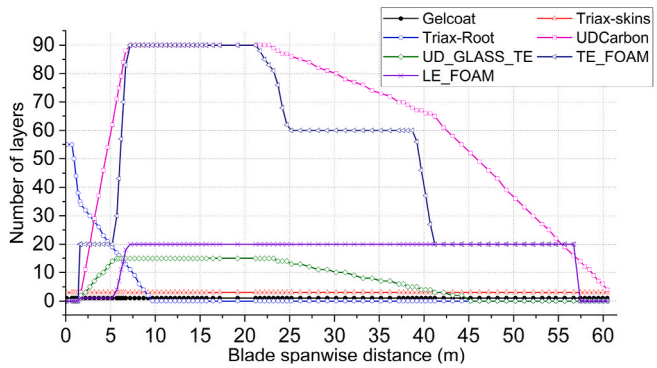

Fig. 10. Number of layers distribution along the blade spanwise for composite laminates.

Table 2
Mesh convergence study for blade FE model under a constant flapwise tip displacement load of 5 m.

Mesh ID	Number of elements	Mesh size (m)	Maximum Von Mises stress (Pa)
1	99878	0.08	1.119E+08
2	**63687**	**0.10**	**1.114E+08 (-0.4%)**
3	44534	0.12	1.064E+08 (−4.9%)

Table 3
Blade mass properties comparisons.

Descriptions	Desired	Resor (2013)	Present Model	Diff to desired values
Mass (kg)	17740	17700	17435.87	−1.71%
Mass center[1] (m)	20.475	19.102	19.79	−3.35%
1st mass moment of inertia[2] (kg m)	3.63E+05	3.38E+05	3.45E+05	−5.00%
2nd mass moment of inertia[2] (kg m^2)	1.18E+07	1.10E+07	1.11E+07	−5.74%

Note: 1. Locate along spanwise direction; 2. With respect to the coordinate origin.

Table 4
Modal frequency comparisons.

Mode #	Frequency (Hz)		Diff	Description
	Ansys (*Resor, 2013*)	Present model		
1	0.87	0.86	−0.77%	1st flapwise bending
2	1.06	1.10	+3.79%	1st edgewise bending
3	2.68	2.72	+1.38%	2nd flapwise bending
4	3.91	3.94	+0.75%	2nd edgewise bending
5	5.57	5.51	−1.00%	3rd flapwise bending
6	6.45	6.36	−1.40%	1st torsion

properly resolve the curvature on the blade surface, as illustrated in a blade cross section view in Fig. 12 (b). The total number of cells is 13.1 million. The numerical specifications applied in both cases are illustrated in Fig. 12 (d).

In the structure participant, as previously mentioned, the multibody dynamics code MBDyn serves as the structural participant in the FSI process, where 49 interconnected nodes are used accounting for the elasticity of the blade structure, additionally, two nodes situated at the rotor centre and the fixed ground. This gives a total number of structure nodes of 149.

5.2. Case 1 – DLC 6.1 load condition

A 50-year wind state extreme condition (DLC 6.1) is analysed (Miao et al., 2019; Resor, 2013). The free-stream velocity of air $U0 = 50\ m/s$, which leads to a blade characteristic Reynolds number of Re = 2.1e+08. Under the cut-out condition of the wind turbine, the rotor angular speed is zero. In Case 1, the instantaneous fluid and structural results focusing at the moment when the blade reaches to its maximum flapwise displacement are analysed in the following sections.

5.2.1. Fluid field results

The detailed CFD results of pressure (gauge) and velocity fields on global X direction are shown in Figs. 13 and 14, respectively. Due to the flow stagnations, a higher pressure occurs on the upstream as the flow approaches to the blade surface, then, a low-pressure region forms on the downstream of the blade, spans from the blade tip to the blade transitional area, where the blade cross section shape is transitioning from circular shape to DU-series airfoils (Resor, 2013), as illustrated in Fig. 13 (b). The local maximum pressure difference occurs at the blade transitional area. With such shape change, a significant flow separation is likely to occur in this area. The streamline plot of the velocity field on X direction justifies the existence of this flow separation phenomenon as illustrated in the streamline plot in Fig. 14 (b). In fact, a low pressure region distribution along the blade, where a swirl structure is formed on the blade downward side and gradually becoming more prominent as it reaches to the blade transitional area of position B.

The distribution of aerodynamic thrust (black curve) and the blade flapwise aerodynamic moment are shown in Fig. 15. Due to the non-uniform shape and dimension variations of the blade profiles along the blade, the thrust is not prominent at first due to the cylindrical profile in this blade region. At the blade spanwise distance of $r/R = 0.17$, a global maximum aerodynamic thrust of approximately 42000 N/m is observed, which is related to a larger cross section chordwise dimension in this blade region. Then, as it further spans to the blade tip, the thrust magnitude decreases.

The flapwise moment on the blade is calculated by firstly multiplying the thrust with the blade sectional spanwise distance r, and then compute the integral of moments from the blade tip to the root. It can be seen that the maximum flapwise aerodynamic moments locates at the root of the blade of approximately 15400 $kN \bullet m$, indicating that the fluid imposes a significant bending moment onto the blade structures.

5.2.2. Stress analysis and comparison

The stress field on the composite blade FE model is established and compared with the results from Miao et al. (2019), where the blade structural dynamics responses from a direct CFD-FEA two-way FSI process are provided. Worth being noted that the present blade dynamic responses are solved with stiffness properties given by NREL official document (Jonkman et al., 2009), which differs from the stiffness properties performed in Miao's study. Due to the absence of available studies that performs FSI analysis with a fully resolved composite material blade, such comparison is acceptable.

The blade dynamics are firstly analysed to assure the accuracy of the stress field. In Fig. 16 (a), the blade maximum tip flapwise displacement is 9.25 m, with a deviation of −9.4% comparing with the results from Miao et al. (2019) of 10.21 m. The present edgewise and spanwise tip displacements are −3.35 m and −1.08 m, respectively. As shown in Fig. 16 (b), the maximum rotational displacement (Euler orientation angle) about the X, Y and Z axis are 0.094, 0.257 and −0.115 radians, respectively. A prominent deviation is observed for the twist angle predictions between the present and Miao et al. (2019), where the maximum twist angle about Z axis is −0.201 radians in Miao's result.

A reasonable agreement is achieved for the comparisons of blade displacement along X direction. This is because the blade shear webs

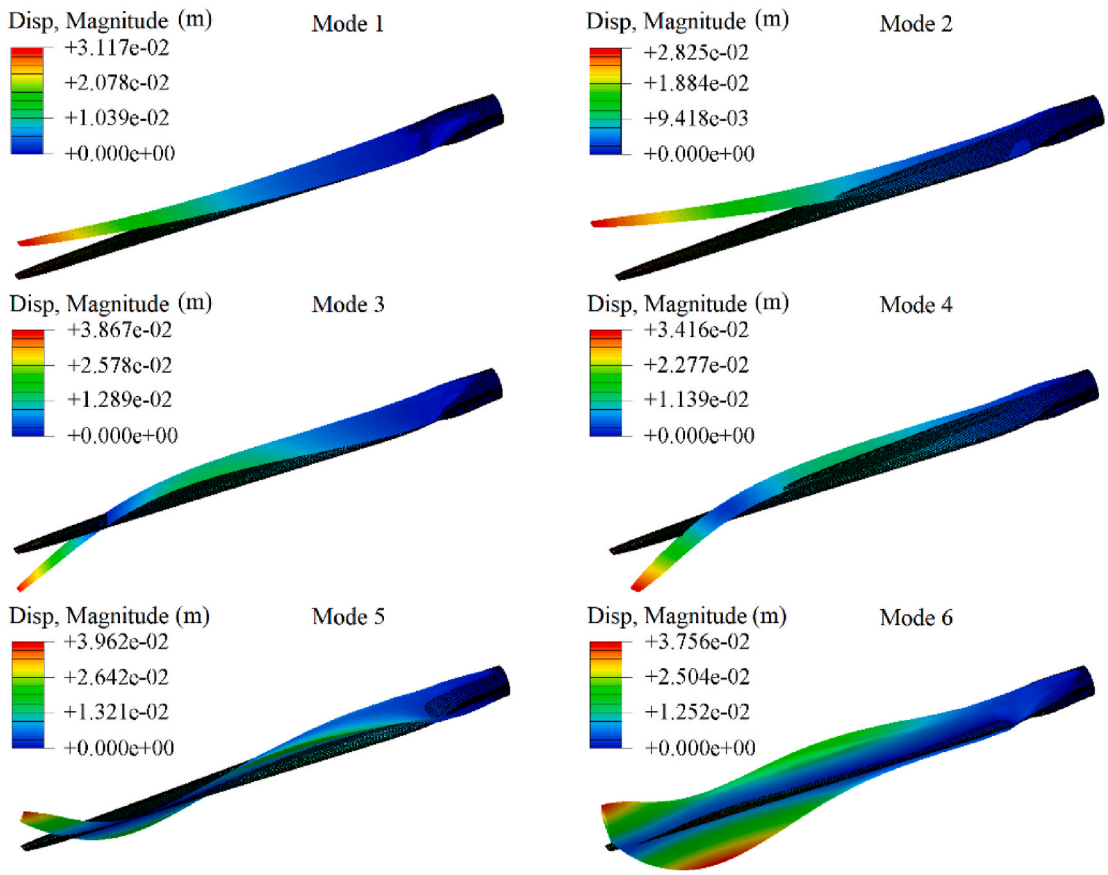

Fig. 11. Modal shapes and frequencies (1–6th modes) of the composite blade FE model, with displacement magnitude contours.

layup are the same in both studies, so that the bending stiffness properties perform similar in terms of enduring the flapwise aerodynamic bending moments. However, the stiffnesses of the blade surfaces composite structures are not entirely identical in two studies, therefore, it is reasonable to observe discrepancies for the blade twisting behaviour as the torsion stiffnesses are primarily affected by the composite structures on the blade surfaces. Besides, different numerical processes of FSI procedures are adopted for solving the complex blade structural dynamics, which may also explain such disparities.

The contours of displacement fields are displayed in Fig. 17. From sub-figure (a) and (b), the flapwise and edgewise maximum displacement are +8.830 m and −3.198 m, respectively, occurring at the tip of the blade. A blade in-plane bending response is observed from Fig. 17 (c), which indicates an occurrence of the strain imbalance where the blade surface in the trailing edge is under tensile loading condition, while the leading edge is experiencing compression loads on spanwise direction.

As analysed previously, the blade transitional region is exposed under a severe aerodynamic drag, causing an accumulated aerodynamic moment especially in the blade transitional areas. Fig. 18 (a) shows the resolved stress field on the composite blade. The stress concentration with a maximum Von Mises stress of 4.198E+08 Pa occurs in the blade root LE_Panel region on the blade suction side, at the spanwise distance of r/R= 0.185 from the centre of the rotor. The concentrated stress comparisons with the literature are listed in Table 5, the maximum Von Mises stress concentration from the literature is 3.964E+08 Pa, occurs at the spanwise distance of $r/R = 0.172$.

To examine the stress distribution more clearly, a Node Path is defined by the intersected edge of the shear web and the blade suction surface. The stress distribution with a local concentration in the blade transitional area can also be observed from.

Fig. 19. The Von Mises stress along the Node Path performs highly nonlinear, which reflects the non-uniform distributions of composite layups and stacking thickness along the blade as can be seen from the thickness distribution plot in blue.

5.3. Case 2 – rated operation condition

A FSI analysis is conducted for the composite wind turbine blade with a fixed bottom configuration, the constant rotating angular speed of $\omega = 12.1\ rpm$, and the incoming freestream velocity $U0 = 11.4\ m/s$, resulting a tip speed ratio (TSR) of $\lambda = 7$ replicating the rated operation condition.

5.3.1. Fluid field analysis

In Case 2, due to the coupling of blade local deformation and global rotation motions, a significant blade nonlinear aerodynamic performance is anticipated. Taking the advantages of the high-fidelity CFD in the proposed framework, we will present the simulated wake vortex structure of the rotor in relation to the time-averaged rotor aerodynamic thrust and pressure coefficient distributions along the blade.

Table 6 compares the converged aerodynamic thrust predictions among the present study and other literatures that uses the same blade geometrical configurations and operation conditions, showing that the thrust is reasonably predicted in our simulations (Dose et al., 2018; Liu et al., 2019; Yu and Kwon, 2014). As illustrated in Fig. 20, a formation of vortex on the blade is observed, suggesting an active flow separation with an intensive transient flowing interaction occurred, especially in the local blade root and tip regions. The contour of q-criterion = 0.05 shows the visual boundary of the vortex, mapped with flow velocity on X direction. The q-criterion describes the relationship between the local vorticity and fluid shear strain and determines the vortical regions in the flow field based on the second invariant of the rate of strain tensor Q.

Fig. 21 illustrates the aerodynamic thrust distributions on the blade

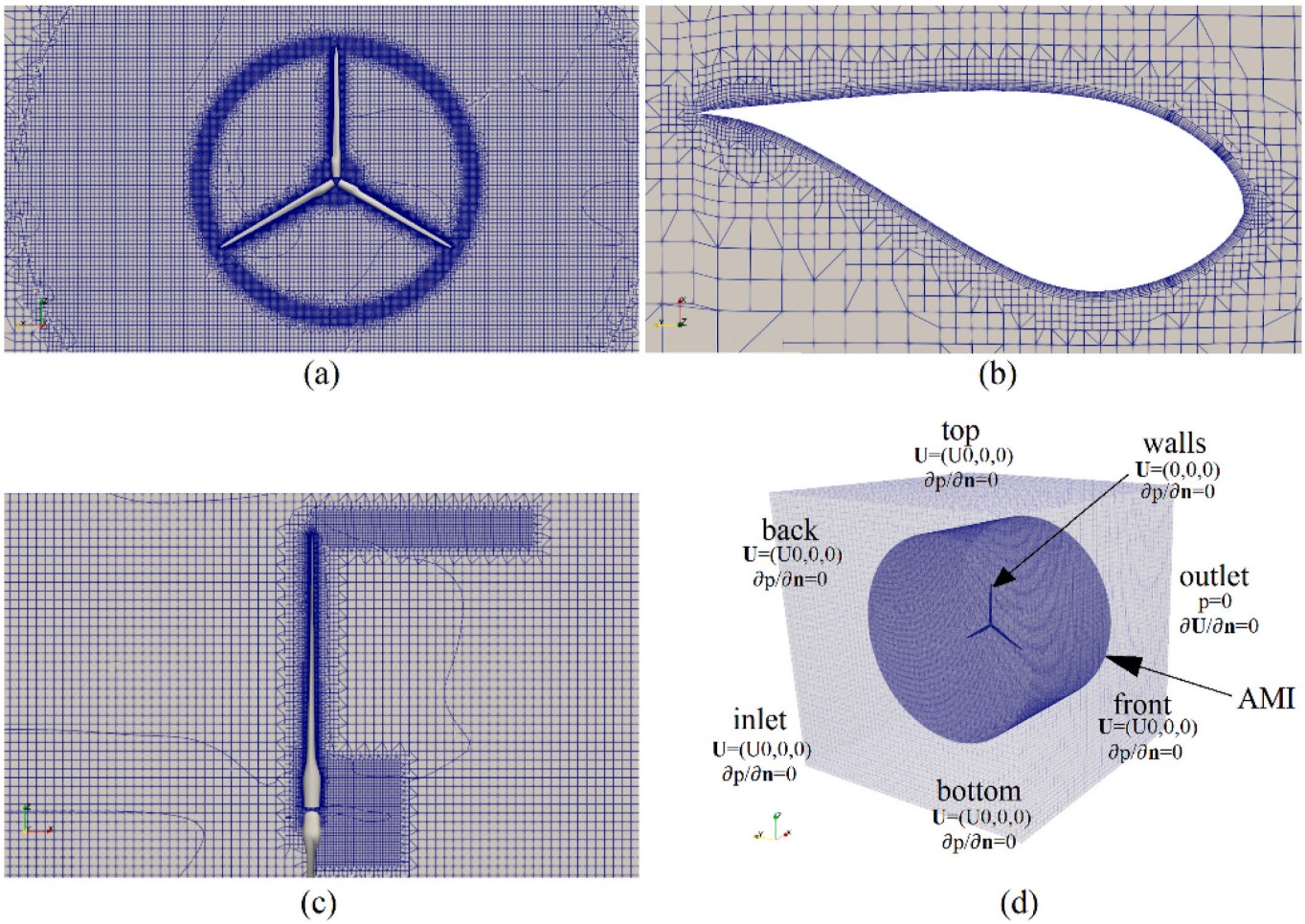

Fig. 12. CFD domain. From (a) X; (b) Z; (c) Y view and (d) the overall mesh.

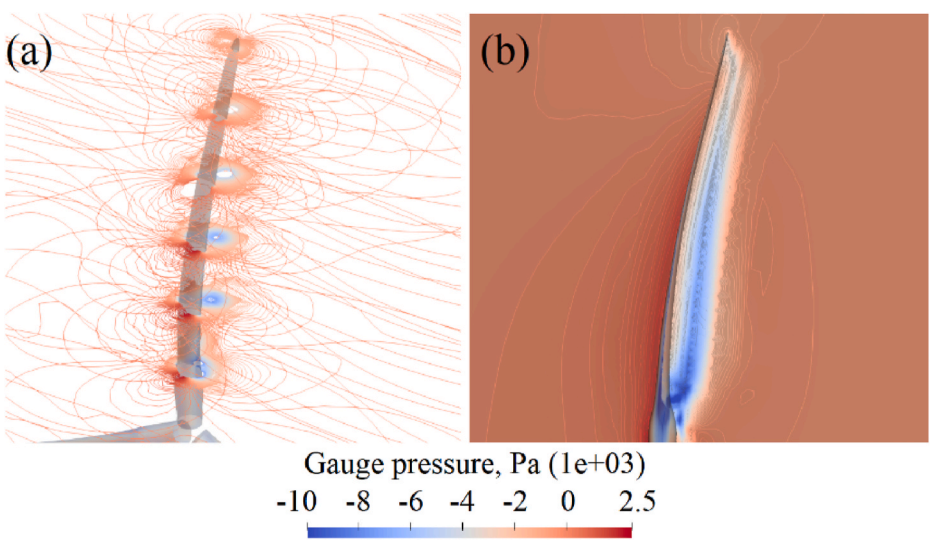

Fig. 13. Gauge pressure contours (a) around the blade, and (b) side-view using a slice plane.

1 at four moments, where the results perform quite similar due to the fully developed flow around the blade during a stable rotation. Meanwhile, a rapid decrease of the local thrust is also observed in the blade tip region where the spanwise distance ranges from $r/R \in (0.9, 1)$.

The streamlines of the fluid X velocity distributed along the blade depict the evolution of such flowing degradation as it spans to the blade tip region. As shown in Fig. 22, the flow closely attaches to the blade surface at $r/R = 0.15$. As the blade tip is approached, the flow detachment with a significant negative X velocity field occurs on the blade suction side near the trailing edge of the blade cross section.

The pressure contours and coefficient distributions on three blade cross sections at r/R = 0.3, 0.6 and 0.9 are presented in Fig. 23, which

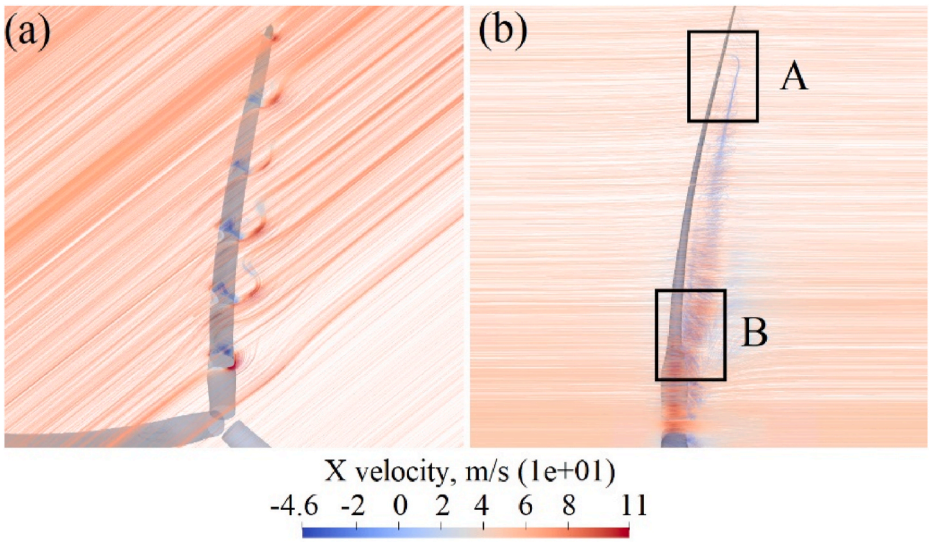

Fig. 14. X velocity field (a) around the blade, and (b) side-view with streamlines.

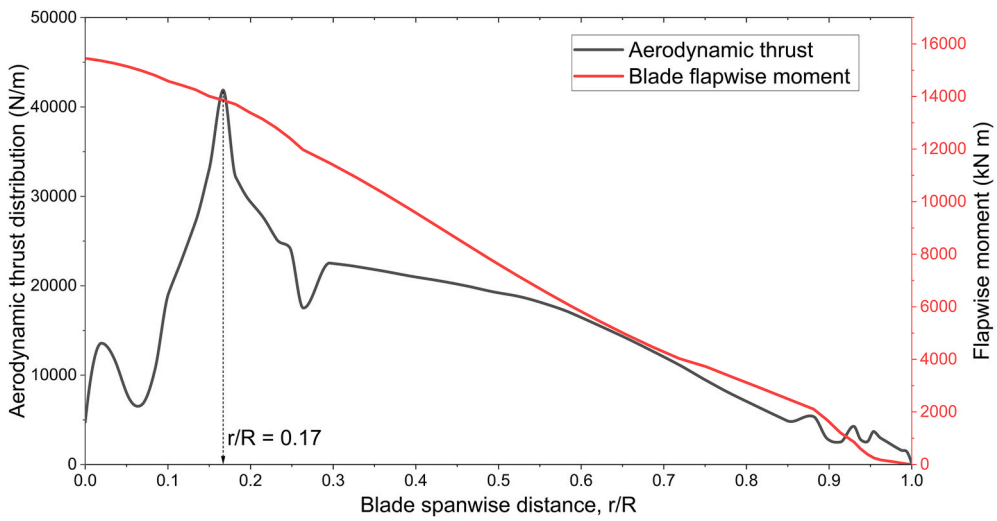

Fig. 15. Blade aerodynamic thrust distribution and the blade flapwise moment, under DLC 6.1 condition.

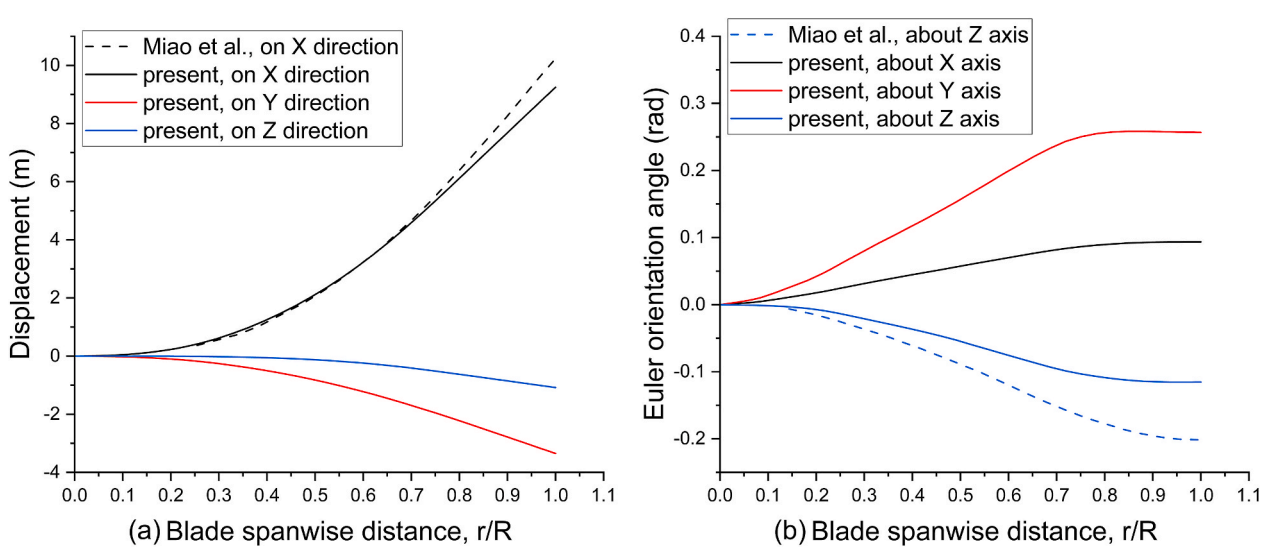

Fig. 16. Blade (a) displacements and (b) Euler orientation angles on the blade section aerodynamic centre, under global coordinate system.

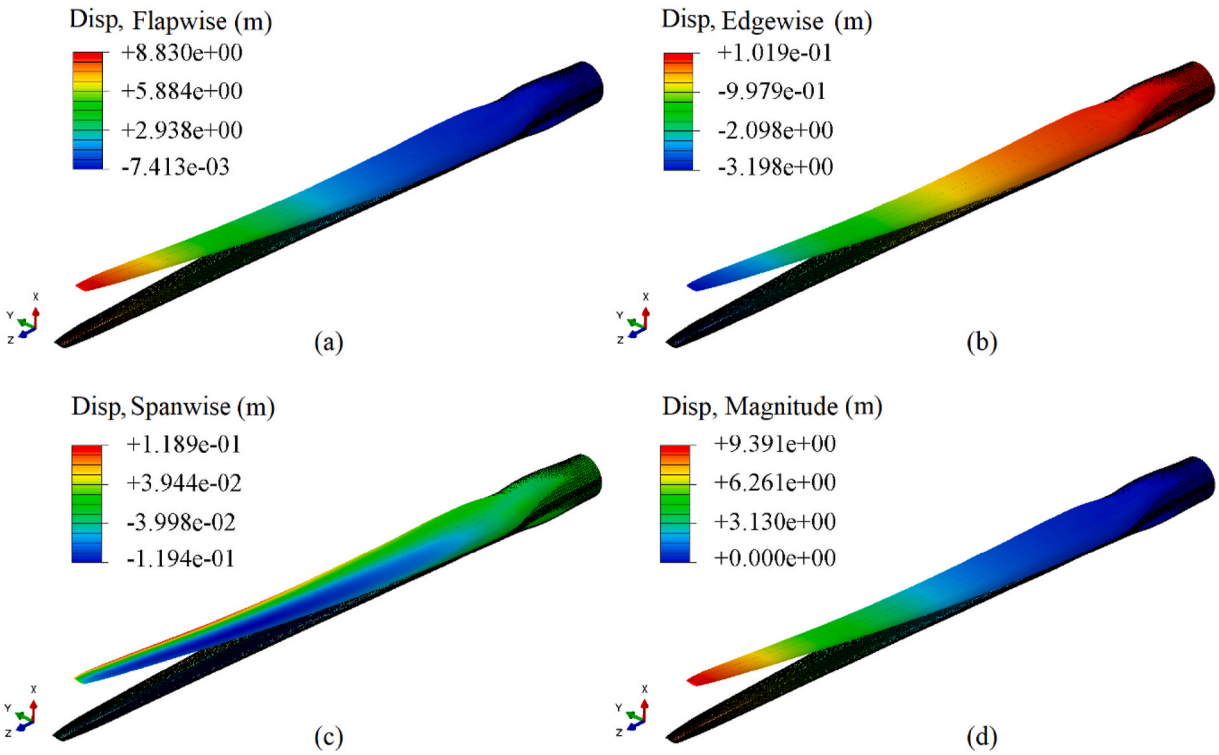

Fig. 17. Translational displacement contours of (a) flapwise, (b) edgewise, (c) spanwise, and (d) displacement magnitude on the composite blade FE model.

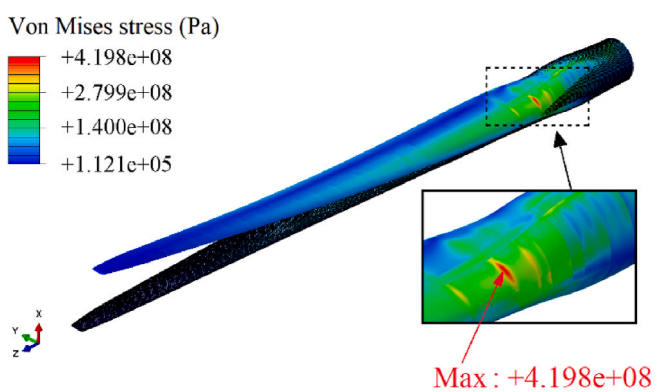

Fig. 18. Von Mises stress field contour on the composite blade surface in Case 1.

Table 5
Von Mises stress comparisons of the composite blade in Case 1.

	Max Von Mises stress (Pa)	Location on blade spanwise, r/R
Present study	4.198E+08	0.185
Miao et al. (2019)	3.964E+08	0.172
Diff	+5.9%	+7.7%

further evident the occurrence of flow separations as is spans to the blade tip. The definition of pressure coefficient C_p is formulated as:

$$C_p = \frac{P_0 - P_\infty}{0.5\rho\left[U_0{}^2 + (\omega r)^2\right]} \tag{11}$$

where P_0 is the local absolute pressure at the blade cross section; P_∞ is the reference pressure which is zero pascal in the present study; ρ is the air density; U_0 is the free stream velocity; ω denotes the rotating angular speed; and r stands for the local spanwise distance of the cross-section airfoil along the blade.

It can be seen from the pressure contour at cross section $r/R = 0.9$, a negative pressure region with adverse pressure gradient is formed near the leading edge on the suction surface of the blade, while it becomes less prominent for the local pressure at $r/R = 0.6$ and 0.3 as the spanwise distance decreases, towards the root of the blade. The non-dimensional pressure coefficient C_p distributions on three cross sections are displayed accordingly. Illustrated by comparing the C_p distributions of the blade cross sections at $r/R = 0.6$ and 0.3, that the local thickness and the shape of the blade cross section may significantly affect the magnitude of blade C_p distribution.

The changing pressure distributions at the leading and trailing edges on the blade cross section profile would result in different local aerodynamic moments, with respect to the local aerodynamic centre of the blade profiles. Therefore, the twist moment of blade sections along the spanwise direction could perform unevenly, so that a persistent non-uniform twist moment is imposed to the blade, which may lead to further structural instabilities of the blade due to the dynamic load balancing between the structure and fluid fields.

5.3.2. Blade dynamics and stress analysis

To analyse the stress field on the blade, as depicted in Fig. 24, four blade azimuth positions of $\alpha = 0^\circ$, 90°, 180° and 270°, during one stable rotation are identified, at corresponding moments of $t = 0T$, $1/4T$, $2/4T$ and $3/4T$, respectively. For simplicity purpose, the dynamics response of blade 1 will be used as the representative to extract the translational and rotational displacements as the boundary condition for establishing the stress fields. Noted that three local coordinate systems are also depicted in Fig. 24 for each blade in the global system.

Due to the periodic aerodynamic loads and gravitational effects to a rotating blade structure, a symmetrical blade deforming distribution pattern is captured in the blade's deformations on Y and Z direction, as presented in Fig. 25 (a2) and (a3). The blade sectional twist about the local Z direction (blade spanwise direction) is shown in Fig. 25 (b3). Starting from t = 0T indicated by the solid red line, the blade twist angle maintains at a low amplitude with small fluctuations among four

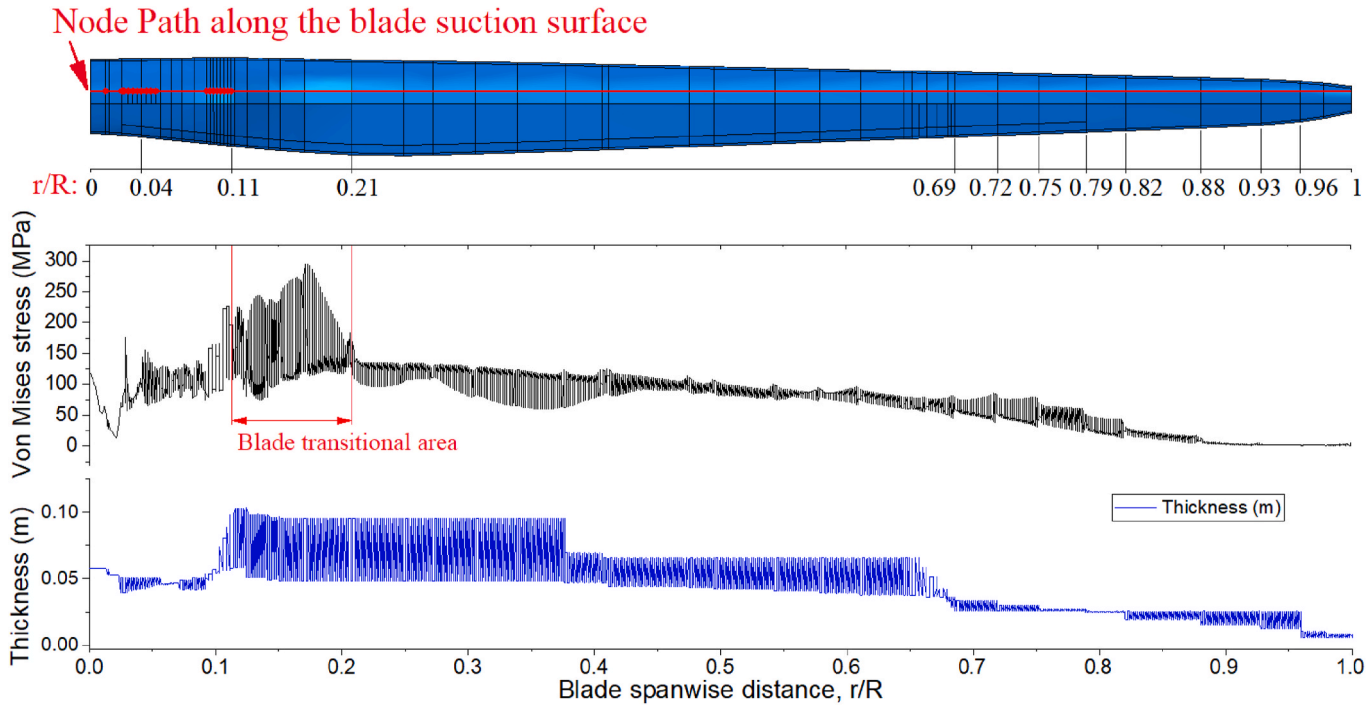

Fig. 19. Von Mises stress distribution along the Node Path on the blade for Case 1.

Table 6
Thrust comparison for the NREL 5 MW wind turbine under rated operation condition.

Flexible blade FSI studies	Thrust (kN)
Present study	**682.5**
Yu and Kwon (2014)	656.4
Liu et al. (2019)	733.0
Dose et al. (2018)	771.3

moments during the stable rotation.

Fig. 26 reveals the relationships among the principal strain and stress on X direction, flapwise displacement and non-uniform thickness distribution on the blade at $t = 0T$ moment. It can be seen from Fig. 26 (a) that the principal strain on X direction on the blade surface with a relatively higher magnitude is mainly distributed within the blade spanwise where $r/R \in (0.121, 0.857)$, on the LE_Panel, Spar Cap and TE_Panel regions, as depicted in green colour. This means a significant higher stress will occur in the corresponding region as can be seen from Fig. 26 (b). While the principal strain on X direction in the blade trailing

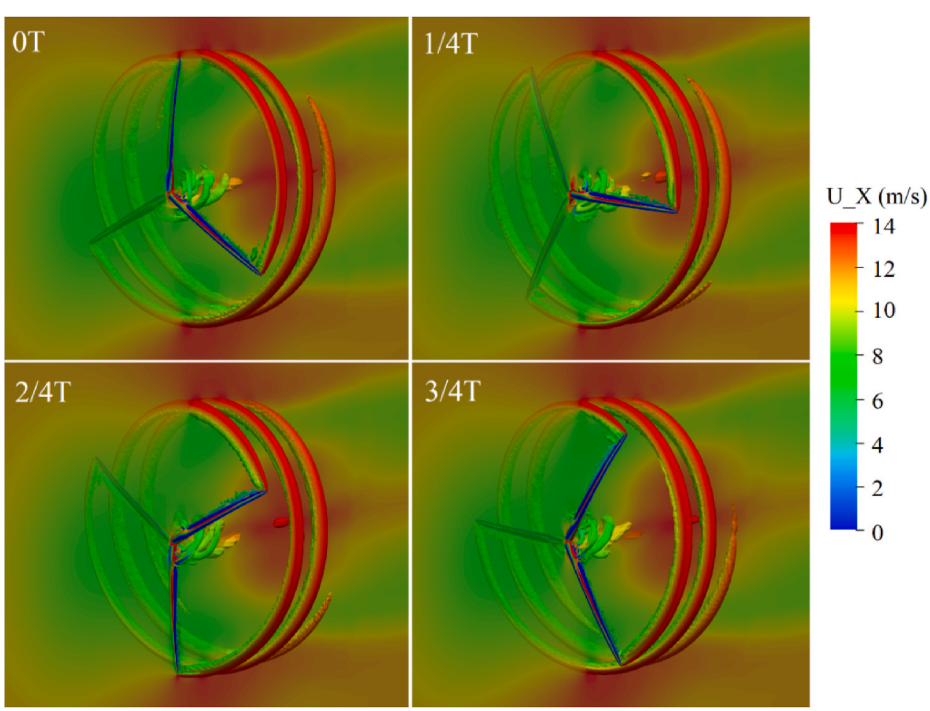

Fig. 20. Instantaneous vortex structures, illustrated by the iso-surface of q-criterion = 0.05 in a complete rotation cycle, mapped with fluid velocity on X direction.

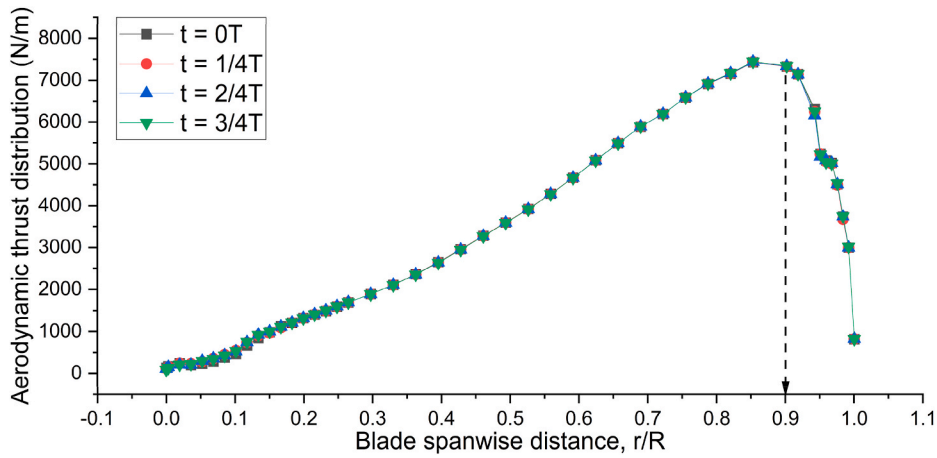

Fig. 21. Blade spanwise aerodynamic pressure loads during the stable rotation cycle, under the rated operation condition.

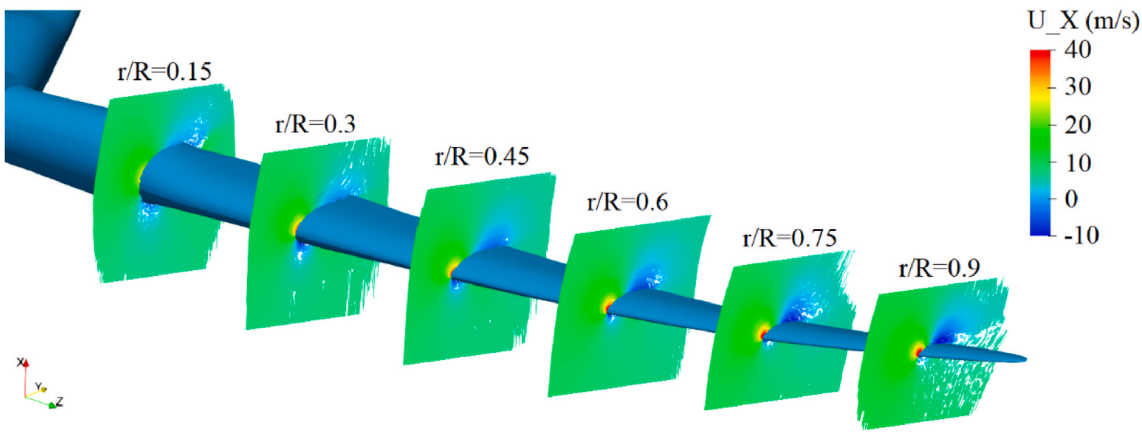

Fig. 22. Streamlines of the instantaneous velocity fields on global X direction (U_X) at $t = 0T$, evenly distributed along the blade spanwise of $r/R \in (0.15, 0.9)$

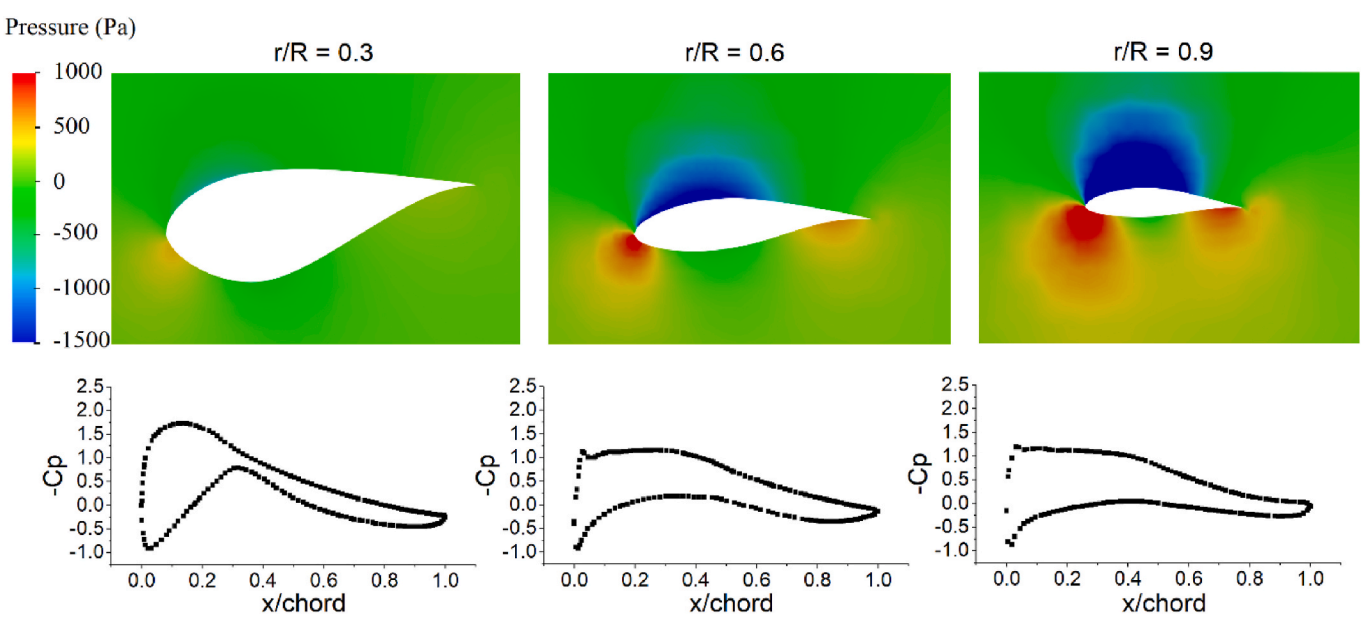

Fig. 23. Pressure coefficient distribution with contour, on the spanwise distances cross section airfoils of r/R = 0.3, 0.6, and 0.9. At $t = 0T$ within a complete rotation cycle.

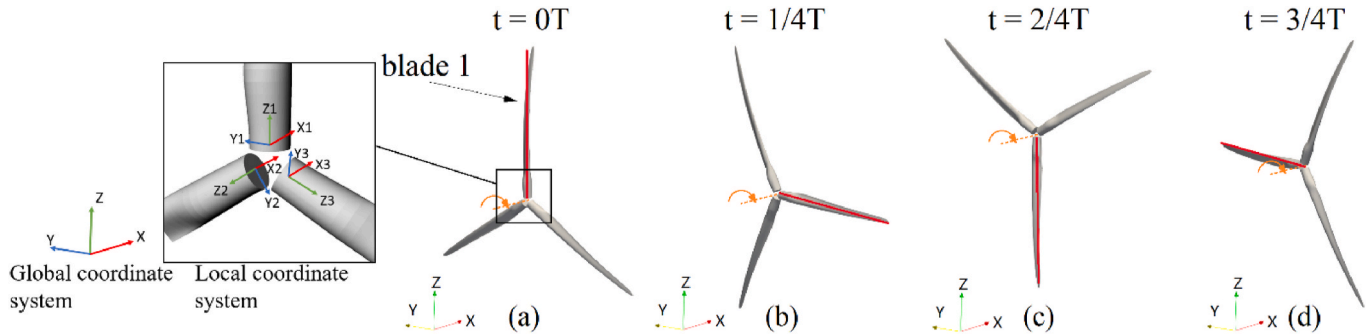

Fig. 24. Four blade key positions (marked in red) for examination of stress fields, at (a) maximum tip displacement position; initial azimuth position of (b) $\alpha_1 = 0^\circ$; (c) $\alpha_2 = 90^\circ$; (d) $\alpha_3 = 180^\circ$; and (e) $\alpha_4 = 270^\circ$.

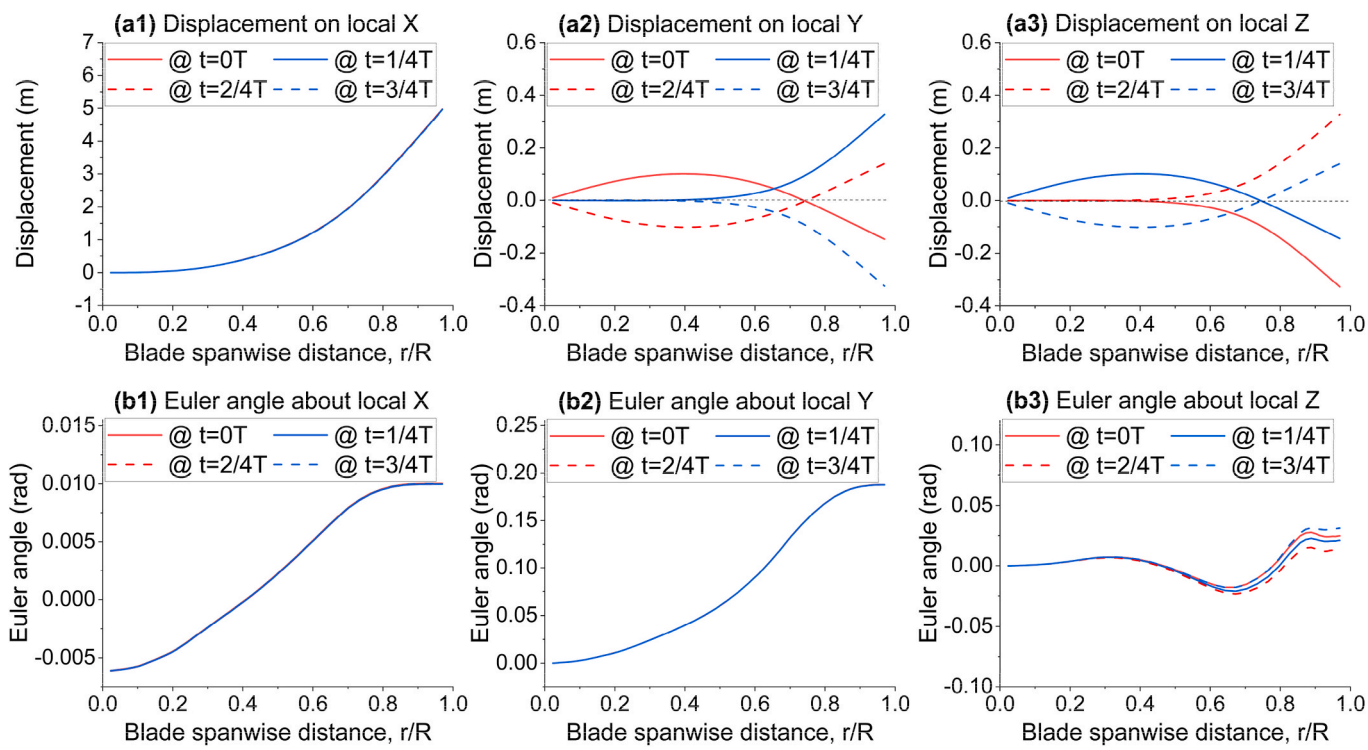

Fig. 25. Blade (a1-a3) displacements and (b1-b3) Euler orientation angles on the blade section aerodynamic centre, under local coordinate systems at $t = 0T, 1/4T, 2/4T$ *and* $3/4\ T$ in a complete cycle.

edge and the blade tip regions is lower, suggesting that a smaller principal stress on X direction will occur in the accordance blade regions.

In Fig. 27, the stress distributions on the blade pressure and suction surfaces are presented. To demonstrate the stress concentration more clearly, the stress distributions on the shear web components are excluded in this figure. During the blade's stable rotation from $t = 0T$ to $t = 3/4T$, the Von Mises stress within the TE_Panel and TE_Reinf areas gradually increases and subsequently decreases. This can be also seen as denoted from 'a' to 'd', a periodic location shifting of the local stress along the blade spanwise in the TE_Panel, TE_Reinf and TE regions is observed on both the blade pressure and suction surfaces.

Such alternating distribution of stress situated in these regions reflects the structural response of the composite blade subjected to the periodic in-plane deformation. As evident from Fig. 25 (a2), it reflects the blade is exposed under a periodic loading condition. This emphases the necessities of partitioning a reinforcement region of TE_Reinf on the blade trailing edge, with reinforced glass fibre laminates employed as the principal load-resistance components within this region.

The stress concentrations of all four moments occur at nearly the same spanwise location within the blade transitional region of the LE_Panel area. During the blade's stable rotation, due to the existence of the coupled effects of in-plane displacement and blade torsion, the maximum stress appears alternatively on both the pressure and suction surfaces during the moment between $t = 3/4T$ to $t = 1/4T$, where the maximum stress shifts to the blade suction surface at $t = 0T$. Throughout the complete rotation cycle, the largest stress concentration magnitude of approximately 8E+07 Pa occurs at t = 2/4T on the pressure surface. The order of predicted amplitude of the concentrated Von Mises stress ranges approximately from 70 to 80 MPa, which indicates a reasonable estimation of the stress on the blade.

The stress concentration on the shear webs is also captured. As shown in Fig. 28, for all four moments, the maximum stresses locate at the blade transitional region, offset to the suction side of the blade surface. During a stable rotation, the maximum Von Mises stress of 1.035E+08 Pa occurs on the shear webs at t = 2/4T. Additionally, a local high stress region is also observed as approaching to the blade tip region, where the spanwise distance of $r/R \in (0.69, 0.86)$ with a lower stress magnitude.

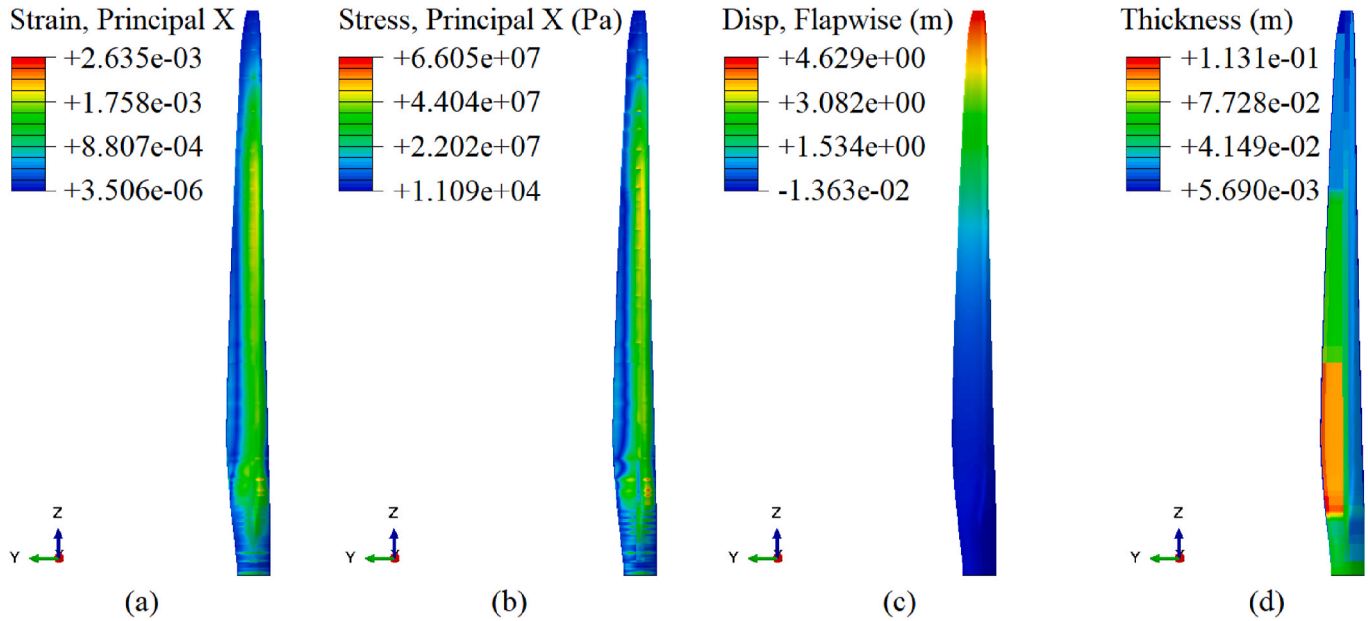

Fig. 26. Contours of (a) principal strain on X direction; (b) principal stress on X direction; (c) flapwise displacement and (d) thickness distribution on the blade FE model, at $t = 0T$ during the blade stable rotation cycle.

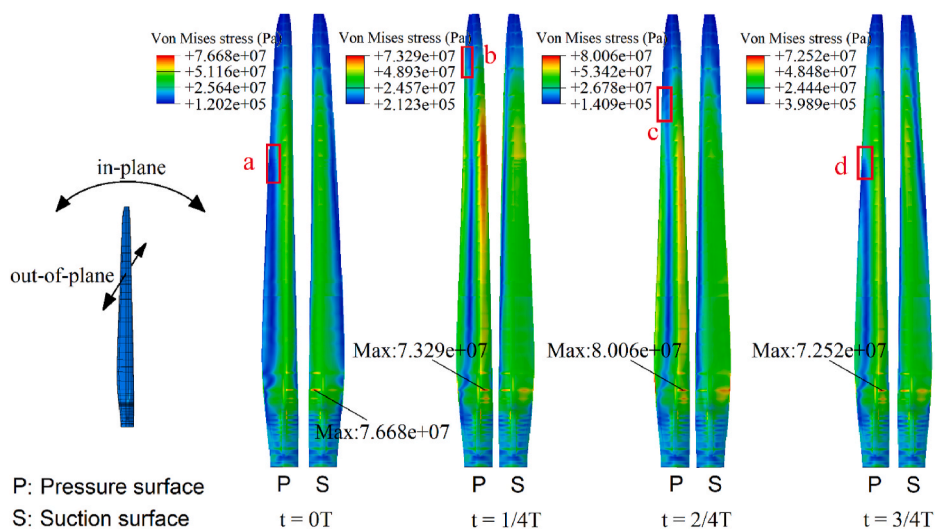

Fig. 27. Von Mises stress distributions on the composite blade pressure and suction surfaces at four key moments during a rotation cycle.

Fig. 29 presented an example of Von Mises stress distributions at four moments on the blade suction surface along the Node Path, as denoted in red line. Combining the stresses and the thickness plots, it is observed that the stress evolution performs highly nonlinear along the blade spanwise direction, which is relevant with the localised structural thickness with a non-uniform distribution.

During the blade stable rotation, the Von Mises stress distributions perform similar in the spanwise distance of $r/R \in (0, 0.11)$, in the blade near-root areas as denoted in region A. In the blade transitional areas where spanwise distance of $r/R \in (0.11, 0.2)$, the Von Mises stress fluctuates significantly, and the Von Mises stress at $t = 0T$ outperforms the stress magnitudes of other three moments, as denoted in region B and C. While in the spanwise distance of $r/R \in (0.67, 1)$, as denoted in region D, the Von Mises stress at $t = 3/4T$ outperforms the other three moments in this area.

It is observed that the locations of the sudden increase of Von Mises stress occurs at the connecting edges of each adjacent blade sections, where the local thickness of the composite structure changes rapidly because of the ply-drops (Jin et al., 2023) of the stackings of composite laminates in the numerical FE model. This reflects a potential localised stress deterioration status as a long-lasting strain imbalance between adjacent blade sections is observed. To further investigate the nonlinear rapid variations of stress on the composite layups with ply-drops, a detailed localised modelling of the corresponding blade sections with solid elements might be necessary. While due to the limitations of the current shell element blade FE model, such detailed inspection of in-ply stress distribution is challenging, and thus is not presented in current study.

6. Conclusions and Remarks

In this paper, an effective numerical framework involving a strong-coupling two-way FSI is proposed, which can be an applicable approach for a series of FSI problem that requires the consideration of the detailed transient aerodynamics and complex composite material configurations.

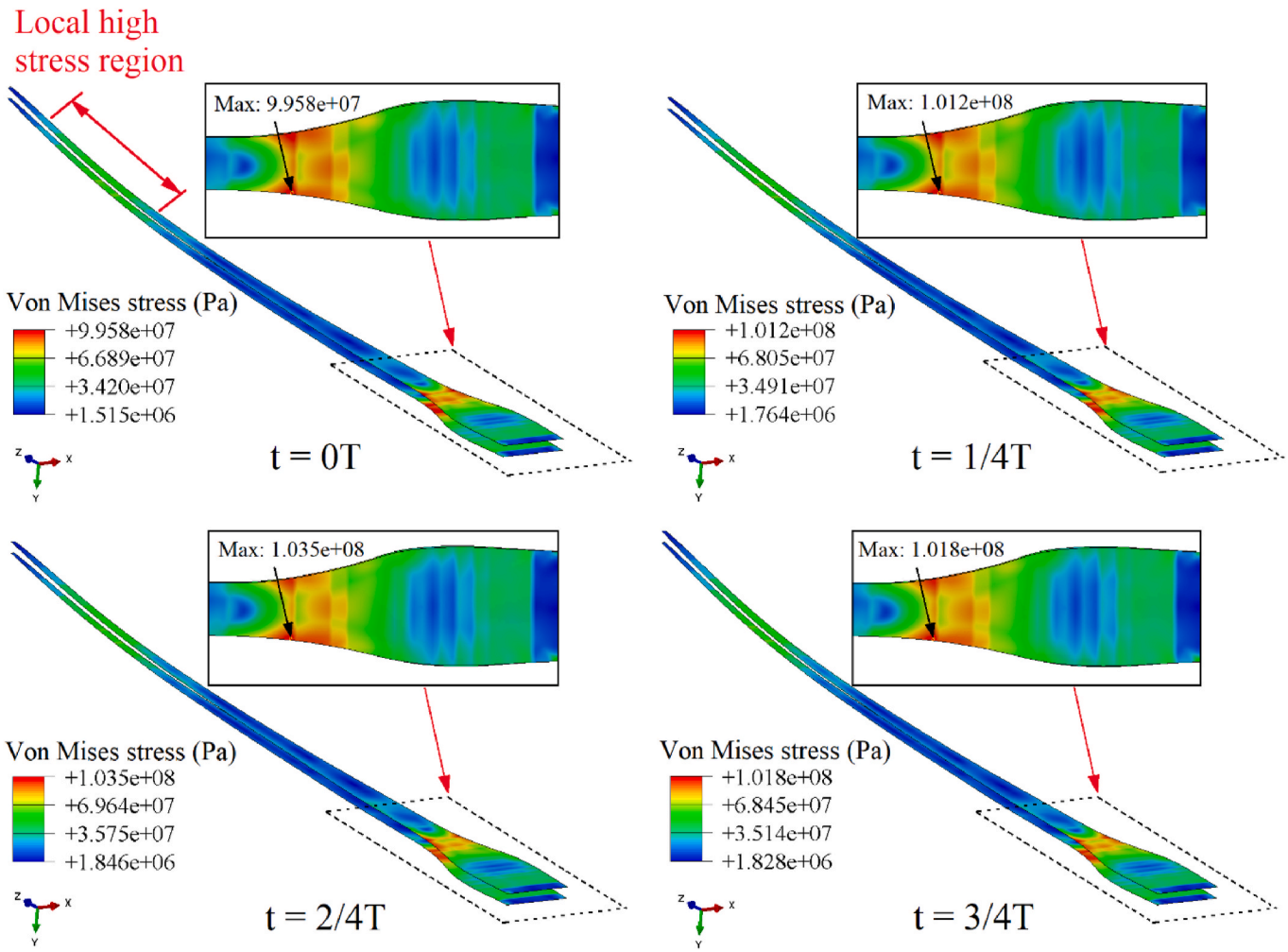

Fig. 28. Von Mises stress distributions on the composite blade shear webs at four key moments during a rotation cycle.

Two case studies have been tested to demonstrate the capability of the proposed framework by resolving the detailed blade aerodynamic behaviours under the operation condition and the stress field distributions on a full-scale NREL 5 MW wind turbine composite blade.

In Case 1, the interacting mechanism of the instantaneous blade kinematics under the aerodynamic load is revealed. It is observed that the aerodynamic bending moment would accumulate in the blade root and transitional areas. This results in a stress concentration in this local blade region. The occurrence locations of the maximum aerodynamic bending moment ($r/R=$ 0.17) and the stress concentration ($r/\ R=$ 0.185) are in close proximity. Meanwhile, a reasonable agreement of the Von Mises stress concentration is observed comparing to the literature results, due to a similar blade bending stiffnesses performance. A promising computational cost reduction of 24.75% is realised using the proposed FSI framework for analysing the same problem. The different HPC computing capacity could be another source of the performance deviations. However, it is considered that the main contributor to this is because the proposed FSI framework avoided the direct surface-to-surface interpolations, which is conventionally being applied in a CFD-FEA FSI process.

In Case 2, considering the rated operation conditions, a thorough blade aeroelastic analysis using the proposed FSI framework is given. The impacts of the blade aerodynamics to the composite structure are revealed. The composite blade Von Mises stress fields at four moments during a complete blade rotating cycle are analysed. Under the realistic aerodynamic conditions, the identifications of the critical locations exposed to the relatively high stress, and intense localised stress fluctuation regions are achieved. A high nonlinearity of stress distribution along the blade spanwise is captured. With our proposed FSI framework, it is found that the factors of the non-uniform thickness distribution, the orthotropic composite properties and the non-consecutive composite stacking configurations on the blade may impact the structural performance significantly and cause a highly nonlinear stress distribution in the composite layers on the blade.

Without modelling the composite blade structure with such fidelity, such as using a beam element model accounting for the blade aeroelastics as the works by Dose et al. (2018) and Liu et al. (2019), the stress status on the blade is challenging to be inspected.

In the future works, improvements can be made to consider the effects of tower and nacelle of the actual wind turbine, so that a more complex flowing interactions of the fluid could be captured, and to achieve more realistic blade aerodynamic predictions. From the structural point of view, the number of blade sections can be increased in the Abaqus (SIMULIA, 2014) FE model, specifically for the potential stress concentration regions, since a rapid stress gradient is likely to occur.

Further extensions of the proposed FSI framework functionalities are possible to unlock the degree-of-freedom of the wind turbine rotor by prescribing the platform motions on a floating offshore wind turbine (FOWT) configuration, so that the composite blade stress status on a FOWT under the more realistic operation conditions can be investigated, which helps forming better understandings of the blade nonlinear aeroelastics under the real offshore environmental state. Besides, the fatigue analysis could also be conducted once the magnitude and location of the stress concentration, and the failure mode of the composites

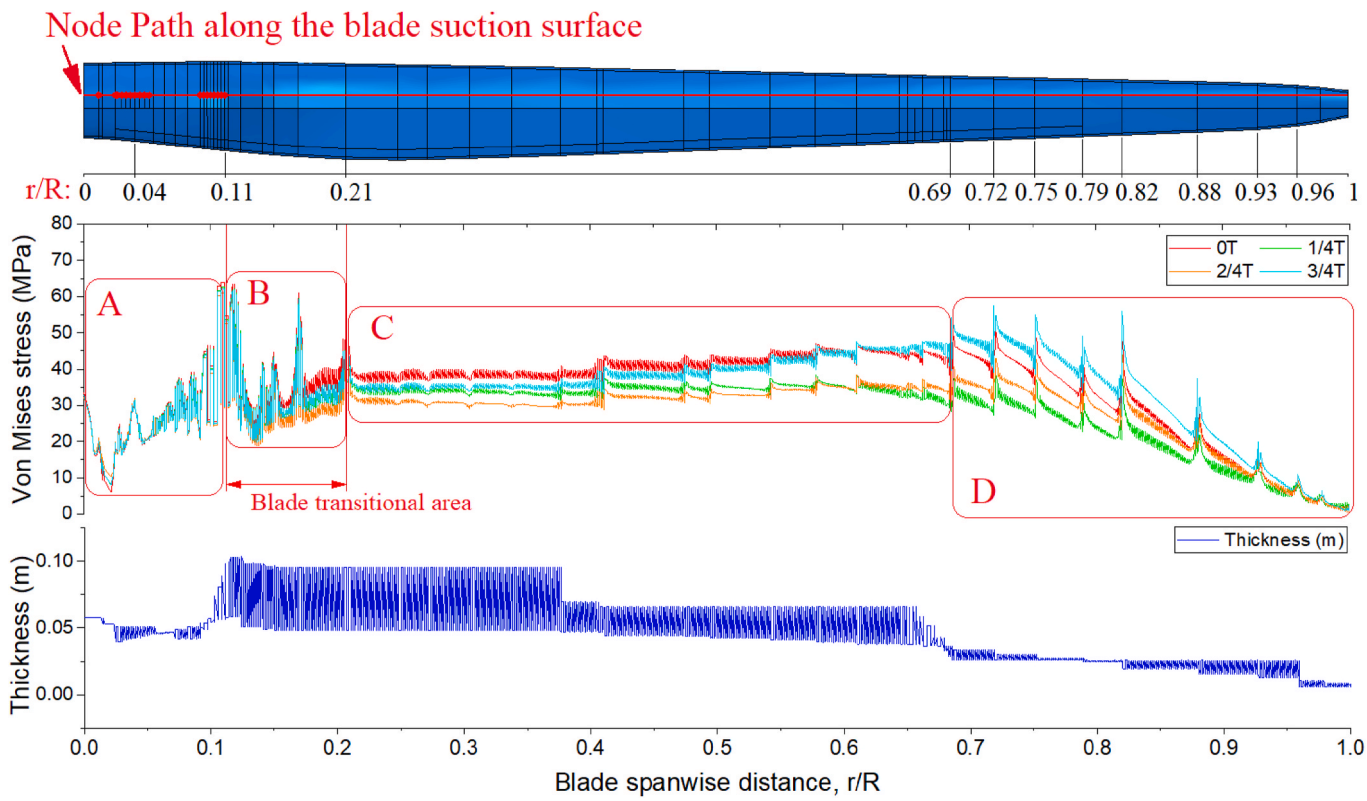

Fig. 29. Von Mises stress distribution along the Node Path on the blade.

are specified.

It is also worthy to mention that the proposed framework is not limited to composite blade application but could also be applicable for other structures that exposed under complex aerodynamic and structural conditions, especially when the coupling effects between multi-physical fields and dynamic motions are involved.

CRediT authorship contribution statement

ZhongSheng Deng: Conceptualization, Methodology, Data curation, Validation, Formal analysis, Investigation, Visualization, Writing – original draft. **Qing Xiao:** Conceptualization, Investigation, Supervision, Resources, Project administration, Writing – review & editing. **Yang Huang:** Writing – review & editing. **Liu Yang:** Conceptualization, Supervision, Writing – review & editing. **YuanChuan Liu:** Methodology, Software, Resources, All authors have read and agreed to the published version of the manuscript.

Declaration of competing interest

The authors declare that they have no known competing financial interests or personal relationships that could have appeared to influence the work reported in this paper.

Data availability

Data will be made available on request.

Acknowledgements

The first author thanks for the High Performance Computing support from the Cirrus United Kingdom National Tier-2 HPC Service at EPCC (http://www.cirrus.ac.uk) funded by the University of Edinburgh and EPSRC (EP/P020267/1) and ARCHIE-WeSt High-Performance Computer (www.archie-west.ac.uk) based at the University of Strathclyde.

Appendix A. Supplementary data

Supplementary data to this article can be found online at https://doi.org/10.1016/j.oceaneng.2023.116412.

References

Bazilevs, Y., Hsu, M.-C., Kiendl, J., Wüchner, R., Bletzinger, K.-U., 2011. 3D simulation of wind turbine rotors at full scale. Part II: fluid-structure interaction modeling with composite blades. Int. J. Numer. Methods Fluid. 65, 236–253. https://doi.org/10.1002/fld.2454.

Carneiro, F.O.M., Moura, L.F.M., Rocha, P.A.C., Lima, R.J.P., Ismail, K.A.R., 2019. Application and analysis of the moving mesh algorithm AMI in a small scale HAWT: Validation with field test's results against the frozen rotor approach. Energy 171, 819–829.

Cesnik, C.E.S., Hodges, D.H., 1997. VABS: a new concept for composite rotor blade cross-sectional modeling. J. Am. Helicopter Soc. 42 (1), 27–38.

Chandar, D., Gopalan, H., 2016. Comparative Analysis of the Arbitrary Mesh Interface (AMI) and Overset Methods for Dynamic Body Motions in OpenFOAM. https://doi.org/10.2514/6.2016-3324.

Chen, H., Yu, W., Capellaro, M., 2010. A critical assessment of computer tools for calculating composite wind turbine blade properties. Wind Energy 13 (6), 497–516.

Cheng, P., Huang, Y., Wan, D., 2019. A numerical model for fully coupled aero-hydrodynamic analysis of floating offshore wind turbine. Ocean Engineering 173, 183–196. https://doi.org/10.1016/j.oceaneng.2018.12.021.

Dose, B., Rahimi, H., Herráez, I., Stoevesandt, B., Peinke, J., 2018. Fluid-structure coupled computations of the NREL 5 MW wind turbine by means of CFD. Renew. Energy 129, 591–605.

Haug, E., 2016. An Ordinary differential equation formulation for multibody dynamics. J. Comput. Inf. Sci. Eng. 16 https://doi.org/10.1115/1.4033237.

Jasak, H., Jemcov, A., Tukovic, Z., 2007. OpenFOAM: A C++ Library for Complex Physics Simulations.

Jasak, H., Tukovic, Z., 2006. Automatic mesh motion for the unstructured finite volume method. Trans. FAMENA 30, 1–20.

Jin, L., Chen, Y., Tang, X., Zhang, J., Wang, Z., 2023. A numerical study on damage characteristics in composite tapered laminates under cyclic loading with different stress ratios. Compos. Struct. 311, 116777 https://doi.org/10.1016/j.compstruct.2023.116777.

Jonkman, J., Butterfield, S., Musial, W., Scott, G., 2009. Definition of a 5-MW Reference Wind Turbine for Offshore System Development.
Lago, L.I., Ponta, F.L., Otero, A.D., 2013. Analysis of alternative adaptive geometrical configurations for the NREL-5 MW wind turbine blade. Renew. Energy 59, 13–22. https://doi.org/10.1016/j.renene.2013.03.007.
Lanzafame, R., Messina, M., 2012. BEM theory: how to take into account the radial flow inside of a 1-D numerical code. Renew. Energy 39 (1), 440–446. https://doi.org/10.1016/j.renene.2011.08.008.
Liu, Y., Xiao, Q., Incecik, A., Peyrard, C., 2019. Aeroelastic analysis of a floating offshore wind turbine in platform-induced Surge motion using a fully coupled CFD-MBD method. Wind Energy 22 (1), 1–20.
Mark, H., Feng, Z., 2023. GLOBAL WIND REPORT 2023. https://gwec.net/globalwindreport2023/.
Masarati, P., Morandini, M., Mantegazza, P., 2014. An efficient formulation for general-purpose multibody/Multiphysics analysis. J. Comput. Nonlinear Dynam. 9, 041001 https://doi.org/10.1115/1.4025628.
Menter, F.R., Kuntz, M., Langtry, R., 2003. Ten Years of Industrial Experience with the SST Turbulence Model.
Miao, W., Li, C., Wang, Y., Xiang, B., Liu, Q., Deng, Y., 2019. Study of adaptive blades in extreme environment using fluid–Structure interaction method. J. Fluid Struct. 91, 102734.
Rahimi, H., Hartvelt, M., Peinke, J., Schepers, J.G., 2016. Investigation of the Current Yaw Engineering Models for Simulation of Wind Turbines in BEM and Comparison with CFD and Experiment.
Resor, B.R., 2013. Definition of a 5MW/61.5m wind turbine blade reference model. https://www.osti.gov/servlets/purl/1095962.
Riziotis, V.A., Voutsinas, S.G., Politis, E.S., Chaviaropoulos, P.K., Hansen, A.M., Madsen, H.A., Rasmussen, F., 2008. Identification of structural non-linearities due to large deflections on a 5MW wind turbine blade. Proceedings of the EWEC, 8, 9-14.
Sayed, M., Klein, L., Lutz, T., Krämer, E., 2019. The impact of the aerodynamic model fidelity on the aeroelastic response of a multi-megawatt wind turbine. Renew. Energy 140, 304–318. https://doi.org/10.1016/j.renene.2019.03.046.
Shabana, A.A., 2020. Dynamics of Multibody Systems. Cambridge university press.
Sharifi, A., Nobari, M.R.H., 2013. Prediction of optimum section pitch angle distribution along wind turbine blades. Energy Convers. Manag. 67, 342–350. https://doi.org/10.1016/j.enconman.2012.12.010.
Simeon, B., 2006. On Lagrange multipliers in flexible multibody dynamics. Comput. Methods Appl. Mech. Eng. 195 (50), 6993–7005. https://doi.org/10.1016/j.cma.2005.04.015.
SIMULIA, 2014. ABAQUS Theory Manual, 130.149.89.49:2080/v6.14/books/stm/default.htm.
Wang, L., Liu, X., Kolios, A., 2016a. State of the art in the aeroelasticity of wind turbine blades: aeroelastic modelling. Renew. Sustain. Energy Rev. 64, 195–210. https://doi.org/10.1016/j.rser.2016.06.007.
Wang, L., Quant, R., Kolios, A., 2016b. Fluid structure interaction modelling of horizontal-axis wind turbine blades based on CFD and FEA. J. Wind Eng. Ind. Aerod. 158, 11–25.
Wang, Q., Zhou, H., Wan, D., 2012. Numerical simulation of wind turbine blade-tower interaction. J. Mar. Sci. Appl. 11 (3), 321–327.
Yu, D.O., Kwon, O.J., 2014. Predicting wind turbine blade loads and aeroelastic response using a coupled CFD–CSD method. Renew. Energy 70, 184–196. https://doi.org/10.1016/j.renene.2014.03.033.
Yu, W., Volovoi, V.V., Hodges, D.H., Hong, X., 2002. Validation of the variational asymptotic beam sectional analysis. AIAA J. 40 (10), 2105–2112.
Yu, Z., Hu, Z., Zheng, X., Ma, Q., Hao, H., 2020. Aeroelastic performance analysis of wind turbine in the wake with a new elastic actuator line model. Water 12 (5), 1233.
Zhang, Z., Zhang, C., Qiao, Y., Zhou, Y., Wang, S., 2023. Design and mass optimization of numerical models for composite wind turbine blades. J. Mar. Sci. Eng. 11 (1), 75.